SPATIALLY RESOLVED PHOTOLUMINESCENCE LIFETIME MAPPING IN THE
VICINITY OF EXTENDED DEFECTS IN SEMICONDUCTORS USING A TIME
CORRELATED SINGLE PHOTON COUNTING SYSTEM AND CONFOCAL
PHOTOLUMINESCENCE MICROSCOPY

by

Timothy S. Mode

A thesis submitted to the faculty of
The University of North Carolina at Charlotte
in partial fulfillment of the requirements
for the degree of Master of Science in
Applied Physics

Charlotte

2016

Approved by:

_____
Dr. Yong Zhang

_____
Dr. Donald Jacobs

_____
Dr. Susan Trammell

ABSTRACT

TIMOTHY S. MODE. Spatially Resolved Photoluminescence Lifetime Mapping in the Vicinity of Extended Defects in Semiconductors Using a Time Correlated Single Photon Counting System and Confocal Photoluminescence Microscopy (Under the direction of Professor YONG ZHANG)

Photoluminescence mapping and time resolved photoluminescence imaging have previously been used to study charge carrier dynamics in bulk semiconductors. Recently, our research group has used spatially resolved PL mapping to examine and model carrier diffusion and recombination in the vicinity of extended defects in GaAs. For the present work a system for obtaining both time and spatially resolved PL images has been developed for closer examination of these phenomena. The system was constructed using a Horiba LabRam 800 confocal micro-Raman system, a time correlated single photon counting (TCSPC) system, and a fast detector which employs a hybrid photomultiplier tube. The system was used to collect photoluminescence lifetime curves for a series of points from a 1-D scan across the defect site. Lifetime data was extracted from single exponential fits of the curves and showed a significant decrease in photoluminescence lifetime in the center of the dislocation. Outside the defect, a slight increase in photoluminescence lifetime and intensity above the background was observed for points very close to the defect (within 2-5 µm). Subsequent CW PL maps made at the same low excitation used for the lifetime measurements revealed a 'halo' around an elongated defect, which was in agreement with the intensity distributions seen in the 1-D lifetime scans from the same region. Lifetime and intensity data are used to construct plots and simple 1-D maps of these quantities vs. position. Carrier diffusion lengths are calculated from carrier lifetimes and the results are compared to diffusion length and

carrier recombination data previously obtained by spatially resolved CW PL mapping, where the carrier diffusion length was assumed to be spatially invariant. Measured photoluminescence lifetimes and corresponding calculated diffusion lengths were found to be much shorter than previously measured values. Alteration of material properties near the defect from high power laser exposure and the low excitation used in making the lifetime measurements are discussed as possibly contributing to both short photoluminescence lifetimes as well as the appearance of the halo effect.

ACKNOWLEDGMENTS

DEDICATION

To my wonderful loving wife and best friend Heather, without whose strength and faith I could not have survived this endeavor. Words can never express my gratitude for what she has done and endured for me. She continues to keep me close to the source of strength that we share; To our beautiful daughter Patia, our most precious gift; may this work benefit her for many years to come.

TABLE OF CONTENTS

CHAPTER 1: INTRODUCTION

The goal of the present work is the development of a system for making time and spatially resolved photoluminescence measurements in a semiconductor sample in order to gain better understanding of the behavior of charge carriers in these materials in the region near an extended defect (ED) such as a major dislocation in the crystal lattice. The effects of ED's are often much more pronounced than those of the common uniformly distributed point defects, primarily due to the large density of defect states associated with the ED. Defect related trapping of carriers greatly affects diffusion patterns of photo-generated electrons and holes, as well as diffusion lengths, carrier lifetimes, and recombination lifetimes. By creating trap states between the valence and conduction bands, these defects deplete the free carriers, and carrier diffusion results in loss of carriers within the carrier diffusion length from the defect site (Gfroerer, Zhang, and Wanlass,2013). As a result, they also affect photoluminescence intensities and lifetimes. A practical model of the processes that occur as a result of these defects may provide advantages in the design of more efficient opto-electronic devices such LED's, diode lasers and photo-voltaic cells. While spatially resolved photoluminescence (PL) reveals much about carrier diffusion in the presence of such defects, time and spatially resolved PL together can provide a more complete picture of carrier dynamics.

The first phase of this study is the development of a system for obtaining photoluminescence lifetime data at points in the area of an ED by use of time correlated single photon counting (TCSPC). The TCSPC system is fitted to a scanning confocal microscope to acquire 1 and 2-dimensional arrays of photoluminescence lifetimes from

which to construct PL lifetime images. Such systems are commonly used to obtain fluorescence lifetime images of biological samples as well as for the study of charge carrier dynamics in materials as in this study, and are usually available as complete turn-key systems. For the present work, a system was assembled from in-house systems and components already in use for Raman and PL imaging microscopy, and from components of a non-imaging TCSPC system that have been suitably modified for the purpose of this research.

The second phase of this study is a test of the system by attempting to obtain PL lifetime data with which to construct images of a sample containing an extended defect for the purpose of tracking carrier diffusion and carrier migration and determining carrier recombination times and carrier diffusion lengths in the area surrounding and including the defect.

1.1   Photoluminescence in semiconductors

Photoluminescence is the process by which a material emits light after being excited by absorbing photons of higher energy than those emitted. An electron in an atom or molecule absorbs the energy of an incident photon and is "elevated" to some higher energy level. After some time, the electron will drop back to its original (initial) state through one or more transitions, one of which may result in the emission of a photon with energy $h\nu = E_{final} - E_{initial}$ (figure 1a). The structure for the energy level diagram for single atoms is quite simple, such as that for atomic hydrogen. Due to overlapping of atomic orbitals, molecular energy level diagrams can become quite complex (figure 1b). In solids, the energy levels "smear" out to form energy bands containing a large number

(on the order of 10^{23}) of closely spaced energy levels such that the band behaves like a

continuous distribution of energies (figure 1c).
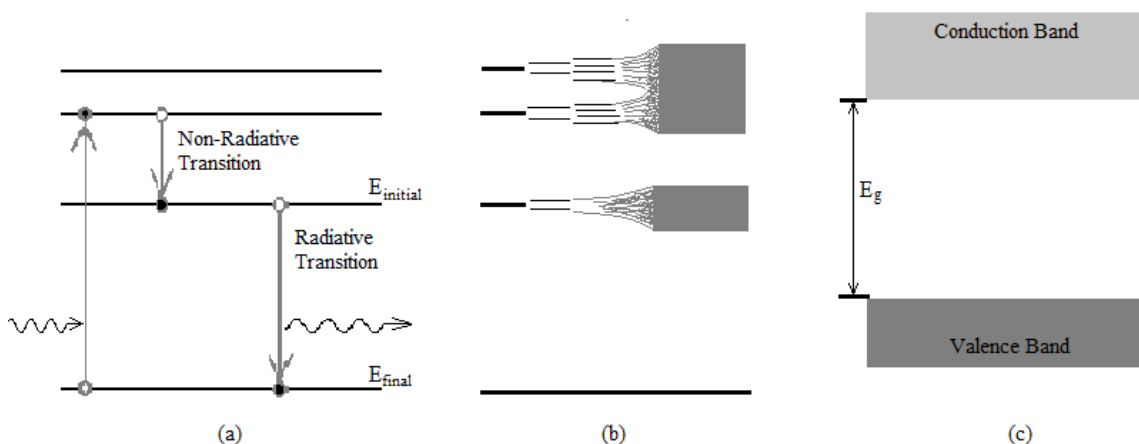
Figure 1: Energy level diagrams a) discrete energy levels of an individual atom, b) The "smearing" of energy levels as atoms of a molecule are brought together, c) Energy bands in a solid (adapted from Fox, 2012)

As more and more atoms are assembled to form the solid, the orbitals of the

outermost, or valence, electrons overlap and their energy levels fuse to form the valence

band (figure 1c). This is the uppermost occupied energy band and is partially filled in

metals and completely filled in insulators and semiconductors. In insulators and

semiconductors, the next higher band, which is the lowest unoccupied band, is called the

conduction band. It is completely empty at zero K. Between these two bands is the

forbidden region called the band gap, with the minimum energy difference between the

bands referred to as the band gap energy (E_g). Normally there are no available energy

states in this region of the band structure (figure 1c).

In the study of solids, particularly semiconductors, it is useful to picture the band

structure in terms of the relationship between the energy of an electron and its

momentum, where the momentum is expressed in terms of the electron wave vector k as

$p = \hbar k$. Figure 2 shows the distribution of energy states in momentum space in accordance with the relationship

$$E = \frac{\hbar^2 k^2}{2m^*}$$

where the quantity m* denotes the effective mass of an electron (m_e^*) or hole (m_h^*), and is required by the fact that neither electrons nor holes behave as free charges in the crystal lattice. The effective mass reflects the influence of the underlying periodic potential of the lattice on the band structure. Figures 2 and 3 illustrate the E-k dispersion for values of k close to zero where the bands are approximately parabolic (Fox, p.116).
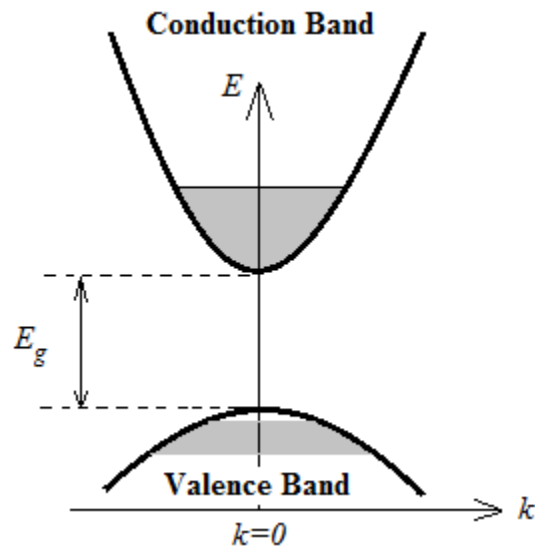

Figure 2: Energy band diagram in momentum space for a direct bandgap material (adapted from Fox, 2nd Ed.).
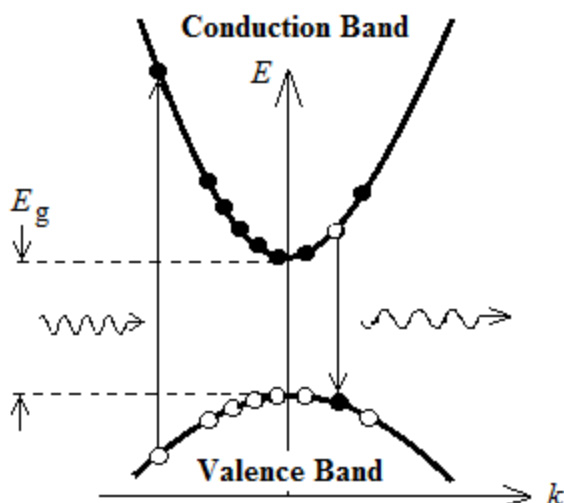
Figure 3: Photoluminescence in a direct bandgap solid. Absorption of photon with energy greater than E_g results in an electron being excited to the conduction band. Emission of photon occurs as an electron in the conduction band falls to an available state in the valence band. Vertical transition arrows indicate momentum conservation (adapted from Fox, 2nd Ed.).

In the case of semiconductor materials, the absorption of a photon results in an electron being excited to a higher energy state which could be in the conduction band, leaving a hole in the valence band. Emission occurs when the electron drops back to an accessible empty state in the valence band, filling the hole and emitting a photon with energy equal to or greater than E_g. This normal mode of electron-hole recombination occurs in the absence of defects or impurities that may generate extra states in the energy gap. The photogenerated carriers may be trapped by these states, which reduces the number of carriers that would normally recombine directly with the holes in the valence band. The trapped electrons will eventually recombine with the holes in the valence band, however, and the process will result either in emitting a photon with energy smaller than E_g or simply emitting phonons or heat to the material. Figure 3 shows schematically the process of photoluminescence in a direct bandgap semiconductor such as GaAs. In

this type of material, the conduction band minimum and the valence band maximum occur at $k = 0$ (figure 2,3). Transitions obey momentum conservation (as indicated by vertical arrows in figure 3) since the momentum of a photon is negligible compared to that of the electron. In indirect bandgap materials, the conduction band minimum and valence band maximum do not occur at the same k point; since the band extrema reside at different values of k, transitions require assistance from of one or more phonons to compensate for the difference in momentum (Fox, p. 79). Indirect bandgap materials such as Si and Ge do not emit enough light for TRPL (Metzger et al., 2004) and will not be discussed here.

Of particular interest to this study is the radiative recombination process, described by the rate equation

$$\left(\frac{dN}{dt}\right)_{Radiative} = -AN \tag{1}$$

where N is the number of electrons in the upper energy state at time t and A is the radiative recombination rate for spontaneous emission (recombination).

Although figure 3 shows radiative recombination of an electron hole pair, a number of non-radiative processes may occur. An electron may lose energy in the form of heat or lattice vibrations by emitting one or more phonons, or, it may transfer its energy to another free electron (Auger processes, Selah and Teich). Of interest here (to the present work) are the effects of defect centers which form "traps". Impurities, surfaces, grain boundaries, and dislocations in the lattice have a profound impact on the recombination process by creating energy levels which lie within the forbidden band gap (figure 4).
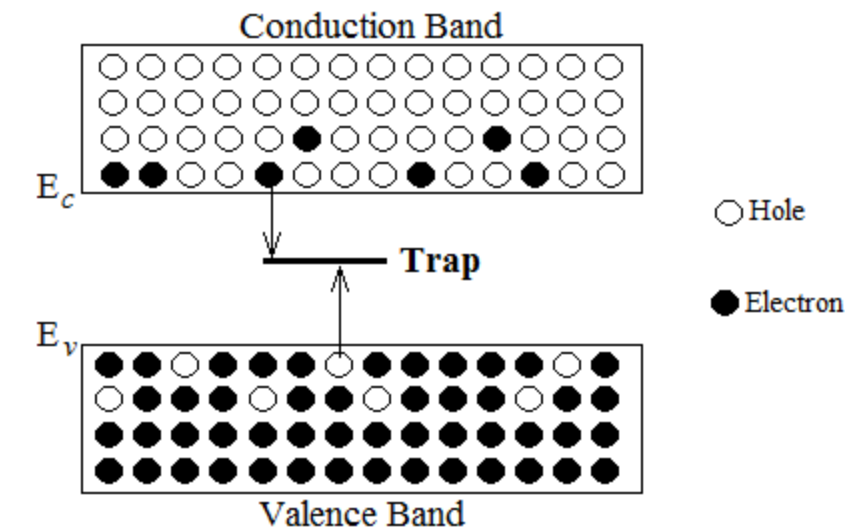
Figure 4: Electron-hole recombination via trap (adapted from Saleh and Teich, p.646).

These intermediate states can lead to radiative or nonradiative recombination if they can trap both an electron and a hole. By increasing the probability of depleting electrons from the conduction bands or holes from the valence band, these trap states shorten the recombination lifetime and increase the recombination rate, and, in the case of radiative recombination, affect luminescence lifetime and yield (Selah and Teich, p. 646). Defects can cause both radiative and non-radiative recombination; however, they most often act as regions of strong nonradiative recombination to the interband radiative recombination of interest. Their presence can reduce the spatially averaged photogenerated free carrier densities and therefore reduce PL intensity of the interband emission near the defect (Fluegel et al., 2014). Carrier density in a given region (that from which PL is being measured) can also be reduced by diffusion of carriers from that region (Gfroerer, Zhang, and Wanlass, 2013). Although the combination of these processes makes characterization of the charge carrier dynamics in such a region difficult, the relationship between carrier behavior and PL intensities and lifetimes can be

generally described in terms of carrier density, carrier diffusivity, and carrier recombination lifetime.

The recombination lifetime τ is a material property and can be expressed in terms of the radiative and non-radiative lifetimes as

$$\frac{1}{\tau} = \frac{1}{\tau_R} + \frac{1}{\tau_{NR}} \tag{2}$$

(Selah and Teich, p. 648). If the lifetimes of non-radiative processes are shorter than those of the radiative transitions, then the upper states will be depleted quickly and little light is emitted. Conversely, if $\tau_R \ll \tau_{NR}$ then the maximum amount of light is emitted. If the system is uniform, the luminescence efficiency η_R can be determined by first incorporating the competing lifetimes into the rate equation

$$\left(\frac{dN}{dt}\right)_{total} = -\frac{N}{\tau_R} - \frac{N}{\tau_{NR}} = -N\left(\frac{1}{\tau_R} + \frac{1}{\tau_{NR}}\right) \tag{3}$$

and then dividing the radiative rate equation by the total rate:

$$\eta_R = \frac{AN}{N\left(\frac{1}{\tau_R} + \frac{1}{\tau_{NR}}\right)} = \frac{\tau_{NR}}{\tau_R + \tau_{NR}} \tag{4}$$

If the radiative lifetimes are known, then the dimensional diffusion length can be calculated from its relationship to the recombination lifetime τ and diffusivity D by

$$L = \sqrt{D\tau} \tag{5}$$

If the material is uniform and uniformly illuminated, the PL intensity at time t takes the same from as the solution to the rate equation

$$N(t) = N_0 e^{\frac{-t}{\tau}} \tag{6}$$

and is dependent on the initial number of carriers (electrons) in the upper energy state N_0 which is in turn governed by the excitation power. Given these parameters, one can get a general estimation of the recombination lifetimes in a material with no defects (or, more commonly, uniformly distributed point defects) provided information on the non-radiative processes is known. However, the material may not be uniform, as with the presence of ED's, and so a method that allows direct measurement of τ at specific locations throughout the sample is used in this study. A spatially resolved map of the diffusion pattern can be obtained from both time and spatially resolved PL measurements. This can provide valuable information on carrier diffusion near extended defects.

1.2   Currently Used Methods for Study of Carrier Dynamics Near ED's.

Several techniques have been employed in the study of charge carrier dynamics near extended defects, including cathodoluminescence (CL), photoluminescence (PL), and laser beam or electron beam induced current (LBIC or EBIC) (Chen et al., 2015). The present discussion will be restricted to PL, and several important configurations will be compared.

Spatially resolved photoluminescence mapping and time resolved photoluminescence (TRPL) imaging have provided a great deal of data regarding the generation, diffusion, and recombination of photo-generated charge carriers in semiconductors. Within these techniques, different geometries for optical excitation and collection of photoluminescence have been demonstrated. Large area uniform illumination combined with local detection (U/L) by means of a CCD camera provides images with spatial resolution limited by that of the camera or diffraction limit.

However, since the photo generated carriers tend to diffuse out to a lower density, resolution is further limited by the diffusion length or illumination spot size, whichever is larger. Large area collection using a CCD to collect a "snapshot" of PL over a larger area is equivalent to performing local detection in parallel from many locations simultaneously. PL from any given location depends not only on the carriers generated at that spot but is also affected by carriers diffusing away from and into the spot. Thus the ability to spatially resolve a defect is affected by the diffusion length.

In the case of local excitation and local detection (L/L) a confocal microscope is used to focus the excitation beam onto the sample and to collect the PL signal (figure 5). Since the excitation aperture and collection aperture are the same in this arrangement, the measured PL comes from the excitation volume. The effect of diffusion is reduced, although still present (because the carriers may still diffuse away from the excitation site), and the spatial resolution is significantly improved compared with the U/L configuration (Chen, et al.,2015). PL data are gathered by scanning a 1-D or 2-D array which contains the defect (figure 6). Further discussion will focus on those techniques that use confocal microscopy.
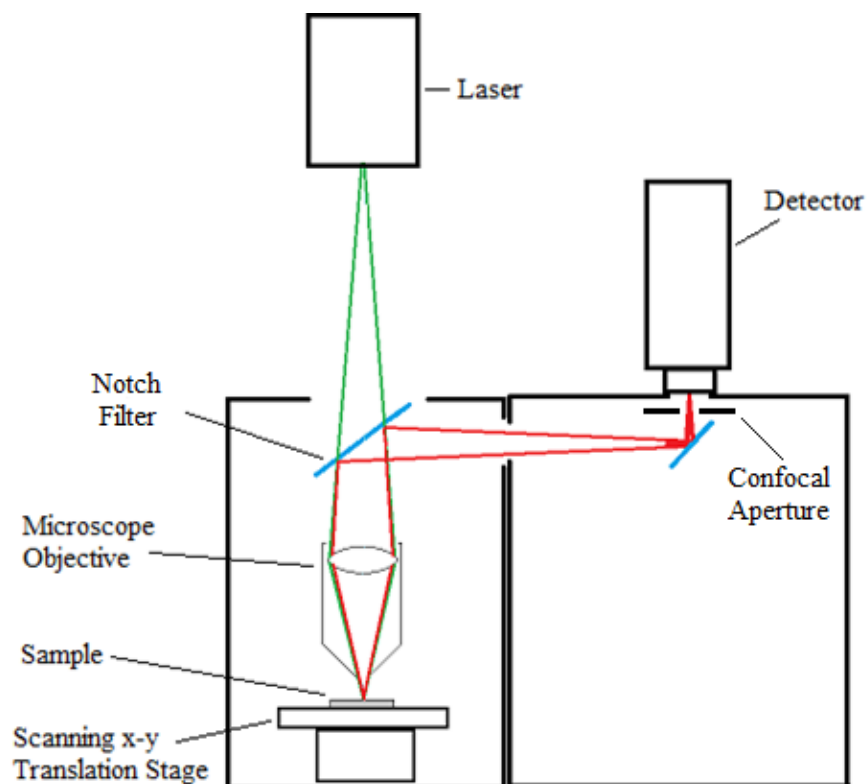
Figure 5: Confocal microscope typical of the type used for Raman and PL microscopy. PL emission from the sample is shown in red.
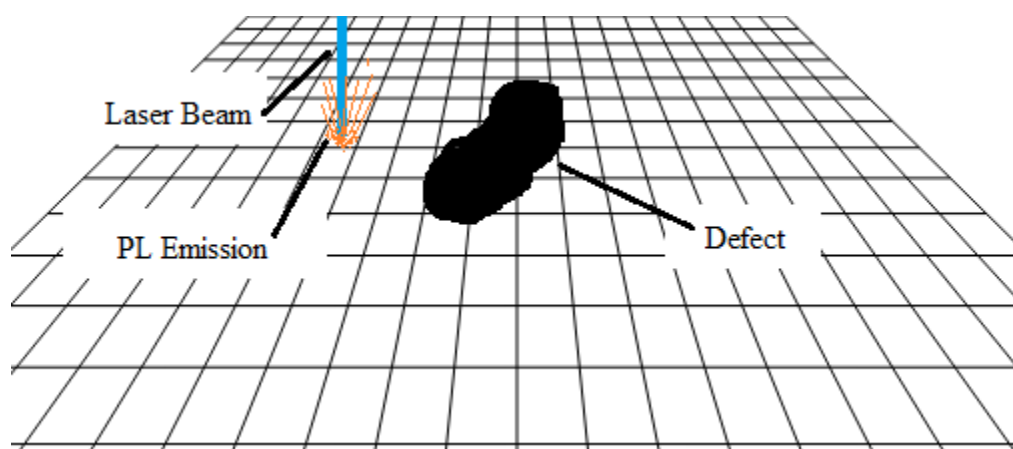

Figure 6: Layout of defect site showing approximate grid for PL excitation and collection. In this local excitation/local collection scheme (L/L) the measured PL signal comes from the excitation volume.

1.3   Photoluminescence Intensity Mapping

Two dimensional CW PL mapping is a valuable contactless procedure for investigating carrier diffusion and recombination in the semiconductor materials. Gfroerer, Zhang, and Wanlass have used this technique to investigate carrier dynamics in the vicinity of ED's in GaAs and have shown that diffusion of carriers to the defect results in a reduction of the PL intensity at points closer to the defect (Gfroerer, Zhang, and Wanlass, 2013). In PL mapping the photoluminescence intensity is measured at locations throughout the sample. The intensity values are then used to construct a false color 2-D image (figure 7). By using a confocal microscope or L/L mode, the effects of diffusion on spatial resolution are reduced. This local excitation/local collection scheme is superior to large area excitation in that the latter only reveals a general reduction in signal in the presence of defects.

This group used a Horiba LabRam HR 800 confocal Raman microscope with continuous excitation at λ=632.8 nm and a 100x objective to achieve a spot size of about 860 nm. The motorized stage of the LabRam is capable of steps as small as 100 nm, leaving the laser spot size as the main limit on spatial resolution. With defects and diffusion lengths measured in microns, the step size and laser spot size are adequate to resolve these features. The images provide contrast data which show areas of carrier loss due to diffusion and non-radiative recombination as dark regions surrounding the defect, which appears as the darkest spot near the center (figure 7). Note the increase in diffusion length with decreasing laser power except at the lowest power, where uniformly distributed point defects serve as background and are capable of grabbing electrons and holes thus limiting their mobility. At higher excitation powers, these point defects

quickly become saturated and no longer impede diffusion. Below a certain threshold

power, point defect traps are not saturated as at higher powers and thus obstruct diffusion

(Gfroerer, Zhang, and Wanlass, 2013). Further investigation of this method by Chen et

al. in 2015 suggest that the decrease in PL intensity near the ED is generally a result of

diffusion to the defect site and not due to other processes such as Auger or Shockley-

Reed-Hall recombination (Chen et al., 2015).

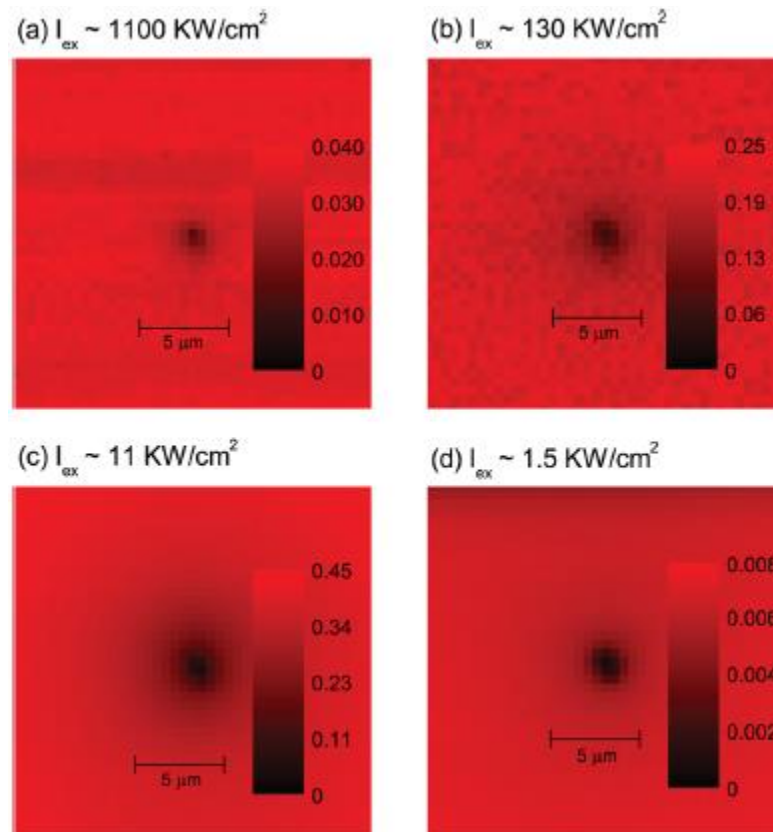
Figure 7: Plan view of confocal PL maps of an isolated dislocation in GaAs over a wide range of photoexcitation intensities I_{ex} (I_{ex} values do not include reflection loss). Greyscale values are estimates of radiative efficiency- the ratio of photons emitted to photons absorbed (Gfroerer, Zhang, and Wanlass, 2013).

1.4   Time Resolved Photoluminescence

From TRPL we get a more direct measurement of the mean time between carrier generation and recombination (FOX, p. 126). A change in the PL decay time near the defect can be the result of loss of carriers by radiative recombination, diffusion, and non-radiative recombination. Time resolved PL measurements alone cannot distinguish between these three processes and therefore cannot provide accurate carrier transport information. However, the use of time and spatially resolved PL mapping can distinguish between these phenomena and allow for closer examination diffusion patterns (Fluegel, et al, 2014).

Incorporating time correlated single photon counting into TRPL enhances these techniques by providing greater sensitivity and greater temporal resolution (B&H handbook, 6th Ed.). Available TCSPC systems are capable of recording PL lifetimes as short as a few picoseconds, while presently available detectors are capable of resolving PL decay curves of less than 200 ps FWHM. Modern pulsed diode lasers (as of the time of this writing) have pulse widths down to 60 ps while commercially available mode locked Ti:Saphire lasers are capable of pulse durations as low as 50 femtoseconds. PL lifetime data is collected much in the same way as with CW excited PL mapping. Instead of intensity only (or contrast data), however, the intensity and PL lifetime are measured at each point scanned on the sample.

1.5   Objective and Technique

The principal goals of this study are to develop a system for obtaining time and spatially resolved PL images of the defect sites which are comparable in spatial resolution to PL maps previously recorded using continuous laser excitation and PL imaging microscopy, and to compare the time resolved data with PL maps previously

acquired by this group for the purpose of possible refinement of existing models for the

diffusion and recombination of carriers near the ED. As in previous PL measurements,

the sample is mounted on the x-y (motorized) translation stage of the confocal

microscope. Short laser pulses are directed through the microscope objective to

illuminate a spot on the sample, the size of which is near the diffraction limit of the

microscope objective, 1.22λ/N.A. The PL signal is collected by the same objective, then

passed through a long pass filter to block any scatter at the laser wavelength. The light

then passes to a fast hybrid photomultiplier tube (PMT) which sends a signal composed

of analog pulses to the single photon counting (SPC) system. The data are recorded by

the SPC system as a series of histograms in the systems memory (figure 8). Post

processing of the data is accomplished by a simple MATLAB^{TM} program which produces

a false color image of the defect site with a color (or contrast) coded time scale.
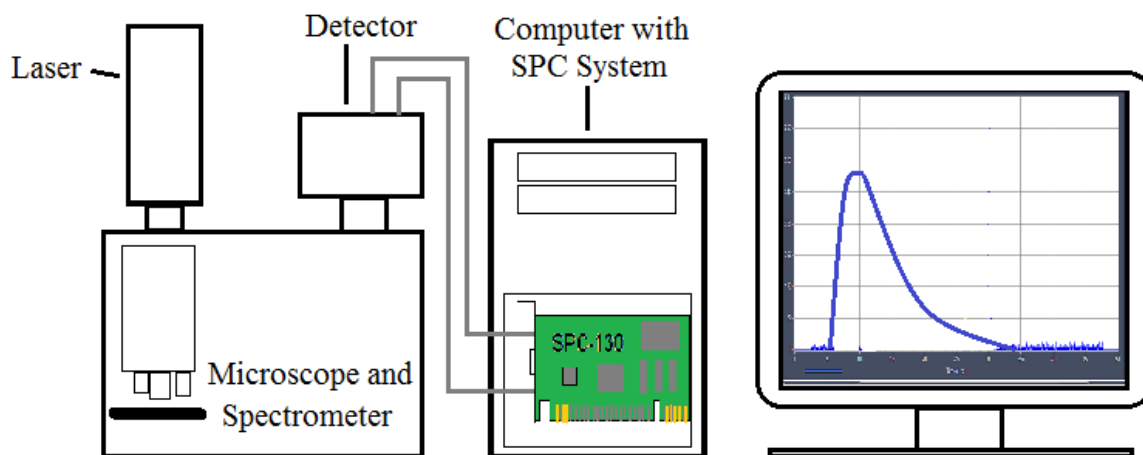

Figure 8: Block diagram of a typical TCSPC system connected to a confocal Raman/PL microscope. The display shows a nominal PL decay curve (a histogram made up of N time channels, where N can be 64, 256, 1024, or 4096 channels per curve). Adapted from the Becker and Hickl *bh TCSPC Handbook*, 6th ed.

CHAPTER 2: EXPERIMENTAL SETUP

2.1   The Confocal Microscope

The Horiba LabRam HR® confocal Raman microscope is typical of the types of

systems used for both Raman and PL imaging microcopy (illustration). The spectrometer

is capable of down to 0.2 wavenumber resolution and has two array detectors used for

Raman and PL microscopy from UV to NIR. As with most modern systems of this type,

the microscope portion can be fitted with a variety of objectives on the rotating turret and

the spectrometer portion can be fitted with a laser line filter, notch filter or long pass

filter, and variable neutral density filters. A stepper motor driven x-y-z stage can be

moved in increments as small as 100 nm. An auxiliary detector port on top of the

spectrometer section consists of an externally threaded tube for mounting PMT, SPAD

(single photon avalanche diode), or other types of single channel detector modules. A

special C-mount adapter was made to attach a Becker and Hickl HPM 100-50 hybrid

PMT module to the spectrometer. The system is also capable of imaging the sample by

means of a 1024 x 512 resolution CCD camera, which aids in locating points of interest

on the sample.

2.2   The TCSPC System

Time correlated single Photon Counting treats the signal from a detector as a

random series of pulses corresponding to the detection of individual photons. Intensity of

the light signal is determined by the number of pulses (corresponding to the number of

photons) rather than the pulse amplitude. As a result, photon counting results are free of

amplitude noise. Although the width of single photon pulses is typically less than 2 ns,

the transit time spread of the pulses in the detector is usually an order of magnitude narrower, making detection of single photon pulses possible. The time resolution is determined by the transit time spread rather than the pulse width. Detection of individual pulses takes place over many equal time periods which are much longer than an individual pulse. The arrival time of the pulse within the detection period is measured, with periods containing several pulses being neglected. Each time a pulse is detected, a "1" is added into a memory location corresponding to the arrival time (figure 9). Each memory location thus represents an arrival time channel. As 1's "pile up" in each channel, a histogram is formed (figure 8) (Becker and Hickl Handbook,6th ed.).
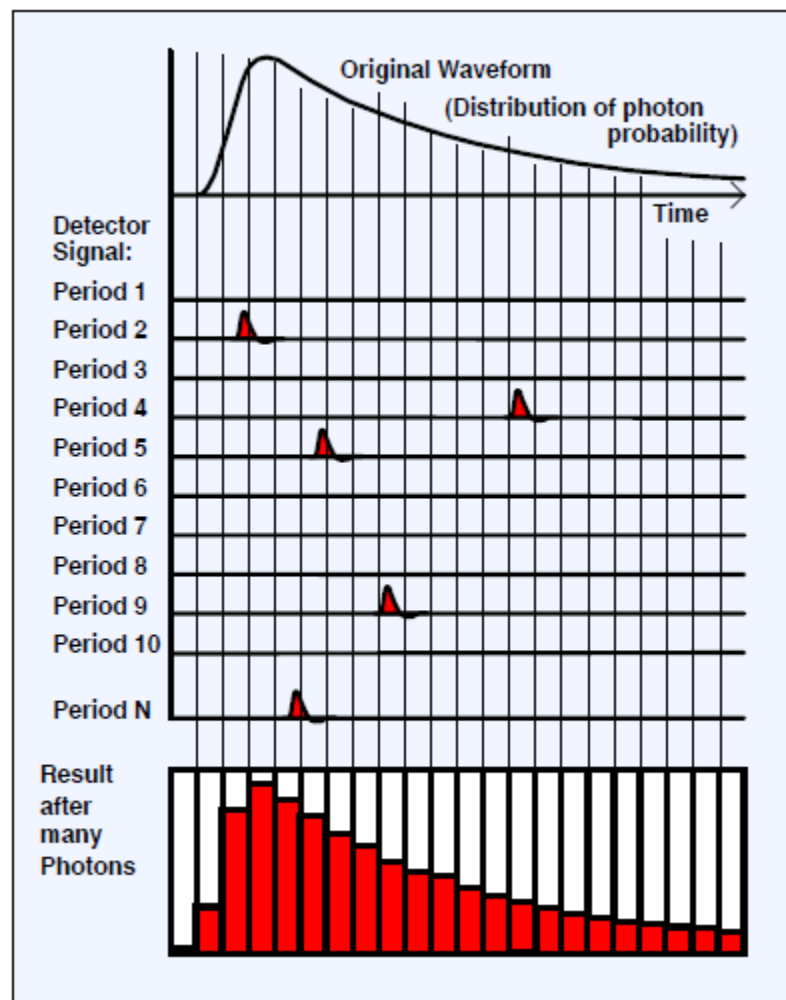
Figure 9: Principle of time correlated single photon counting. Individual photon counts accumulate in time channels which correspond to the arrival time of the pulse, thus creating a decay curve histogram (adapted from Becker and Hickl TCSPC Handbook, 6th ed.)

The Becker and Hickl SPC-130 is a complete system for recording fast light signals by time-correlated single photon counting (Becker & Hickl Handbook, 2014). The entire system resides on a single PC board which plugs into a PCI slot of any modern PCI bus computer. A proprietary analog to digital conversion process (ADC) and a time-to amplitude converter (TAC) makes faster signal acquisition and processing possible, with a theoretical time channel width of <1 ps. External electronics (such as detector,
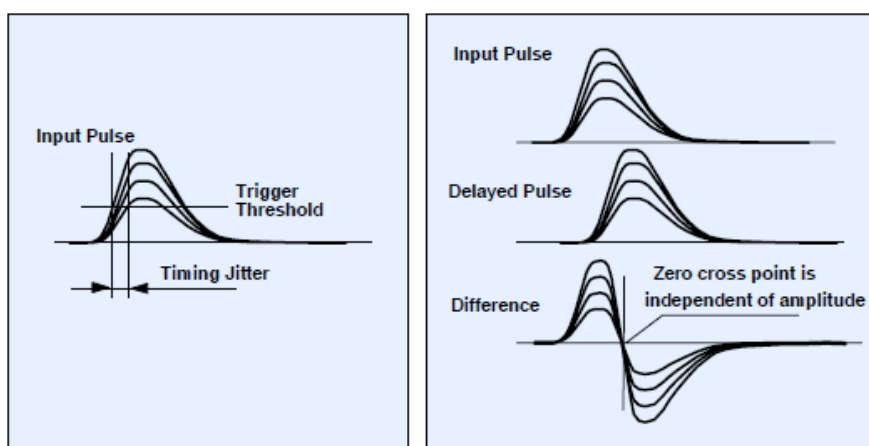
Figure 10: Constant Fraction Discriminator Input for SPC-130. The image on the right shows how amplitude jitter can introduce timing jitter. Left: the reverse start-stop triggering scheme greatly reduces timing jitter (Becker and Hickl Handbook, 6th ed.).

amplifier, signal and sync cable length), however, may limit time resolution to several picoseconds. The triggering scheme for the system is based on a "reverse start-stop principle which allows for pulse sampling rates greater than 150 MHz. Normally, variations in light intensity per pulse and noise in the amplifier stage of most detectors mean that the single photon pulses will have significant amplitude jitter. The amplitude

jitter introduces timing jitter, even if a leading-edge discriminator is used to control the threshold level at the input. For this reason, a constant fraction discriminator (CFD) is used on both the signal and the sync inputs. Constant fraction triggering is accomplished by adding the input pulse to a delayed and inverted copy of the input pulse and using the zero-crossing point as the time reference (figure 10). The CFD also rejects pulses of amplitude lower than a threshold value set by the user allowing for optimization of triggering and photon counting. The TAC then measures the time between detection of an input pulse from the detector and the next sync pulse. This is the reverse start-stop process discussed above. The ADC then converts the TAC signal to a numerical value which is stored in memory. Up to 4096 time channels are available in memory with 32 curves per TCSPC channel.

The SCP-130 system is used in conjunction with the Becker and Hickl DCC-100 detector control card. This unit provides control voltages for gain, sensitivity, sync control, signal and sync threshold values, and allows the user to turn the PMT high voltage on or off through the provided software.

The Becker and Hickl HPM-100-50 hybrid PMT detector module was chosen for its sensitivity and short response time. The PMT has 3 mm diameter GaAs cathodes and a sensitivity range from 340 to 900 nm (bh TCSPC Handbook, 6th ed.). The instrument response function (IRF) of the detector used in this study, which is a convolution of the laser pulse with the detector response, was measured at 178 ps FWHM using a 60 ps pulsed diode laser (SN 755 280 test report). This self- contained system has built in high voltage power supply and preamplifier. Another attractive feature of this detector is its built-in overload protection, which shuts off the high voltage to the PMT if the light

intensity or gain exceed a predetermined "safe" value. A single 15 pin D connector is provided for control of the detector via the DCC-100 module. The output signal comes from a female SMA coaxial connector.

2.3   The Pulsed Diode Laser

The laser available for this study consists of the PicoQuant LDH 440 pulsed diode laser head and PDL-800 pulsed diode laser driver. The average output power of the laser is approximately 0.550 mw at 40 MHz at a wavelength of 445 nm. Pulse energy is about 1.39×10^{-11} J/pulse. Pulse duration is less than 70 ps at the maximum repetition rate of 40 MHz. The repetition rate is adjustable in increments of $^1/_2$, $^1/_4$, $^1/_8$, and $^1/_{16}$ the maximum. The driver provides a synchronization signal that matches the laser repetition frequency. A low pass filter (cutoff at 450 nm) was used in the Raman system in place of the usual notch filter to transmit PL while blocking Rayleigh scatter at the laser wavelength.

Because of the large beam divergence and elliptical beam profile of the diode laser, a small acrylic cylindrical collimating lens was used to make the beam nearly circular. This lens is of the same type used in laser pointers and provided good collimation as can be seen in figure 11. Spot size at the point of entry into the confocal Raman system was approximately 2 mm and the average power going into the system was measured to be 0.5 mw. Initial attempts to achieve a Gaussian beam by coupling into a single mode fiber resulted in a significant loss of power to the point at which a useful PL signal could not be measured. After collecting data with free-space laser coupling, continuing efforts are being made to develop the fiber coupling system.
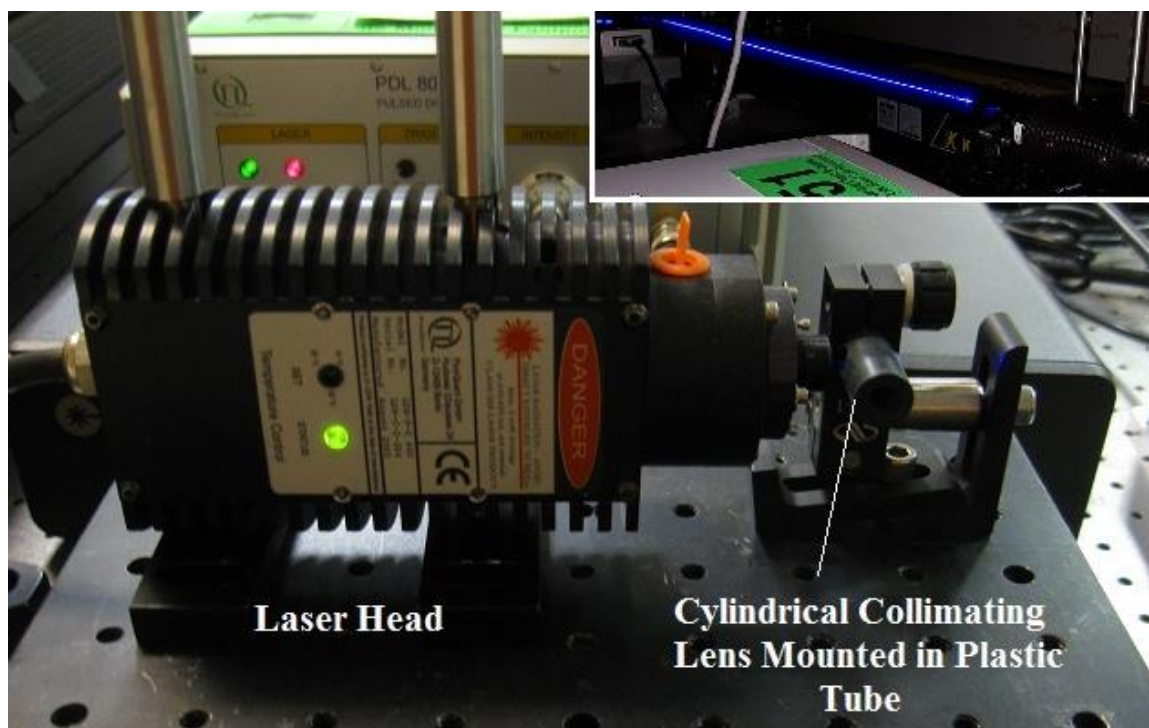
Figure 11: 445 nm pulsed diode laser head showing cylindrical collimating lens in custom mount. Laser power supply is visible in background. Inset: Time exposure showing collimated beam.

2.4   Configuration

Because the SPC-130 is not an imaging system for TCSPC it contains no interface for controlling the stage of the confocal microscope through the SPC system. However, an additional stepper motor controller is available, along with software libraries for the development of user-specific software (Becker and Hickl Handbook, 6th Ed.) Also, pinout diagrams and control signal information are provided in the documentation so that an experimental motor control and synchronization interface for the SPC-130 could be constructed at minimal cost. Upon demonstration of the ability of this system to perform PL lifetime mapping (and possibly imaging) of suitable resolution, efforts to automate the system for reduction of data acquisition time will continue. For the measurements made

here, the two systems were operated independently by "manually" moving the stage through the microscope control software and acquiring the PL lifetime data separately through the SPC system software running on a separate computer. A block diagram of the system is shown in figure 12.
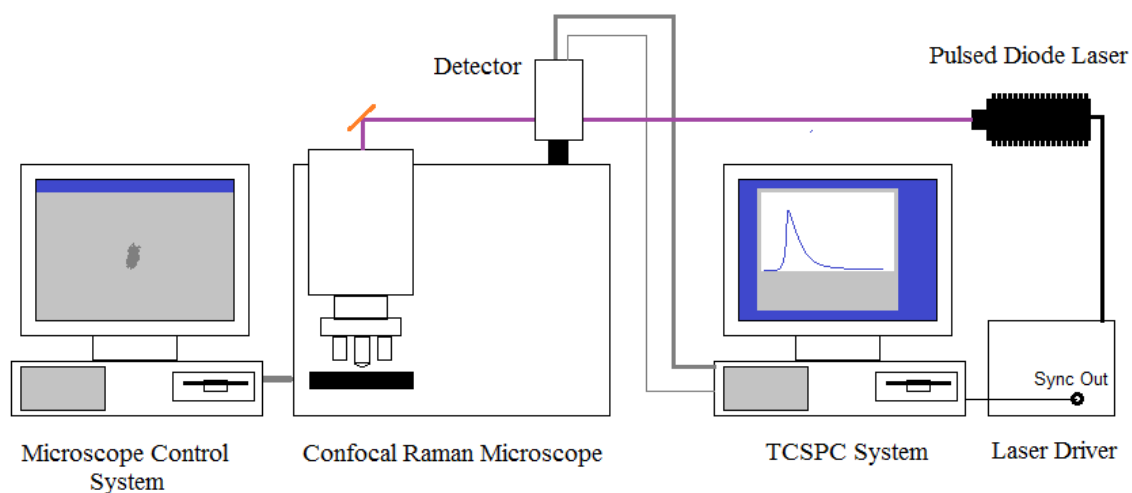

Figure 12: Complete experimental arrangement for obtaining PL lifetime data using confocal microscope and TCSPC system.

CHAPTER 3: EXPERIMENT AND RESULTS

3.1 Description of the GaAs Sample

The sample containing the defects to be studied (designated 1499N) consists of a roughly 1×1.5 cm section of a GaInP/GaAs/GaInP double heterostructure on a 350 µm thick semi-insulating GaAs substrate (figure 13) grown by metal-organic vapor phase epitaxy (MOVPE) (Chen et al., 2015). The 100nm thick GaInP layer absorbs strongly in the blue region of the spectrum which reduces the excitation power to the defect laden GaAs layer. Given the modest power of the 445 nm pulsed laser, this made alignment of the laser critical.
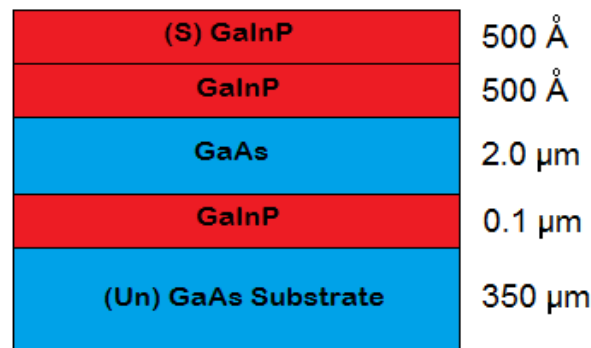
Figure 13: Structure of GaAs sample designated 1499N (image courtesy of Fengxiang Chen).

Prior to making measurements on the sample, a small piece of bare GaAs was placed on the microscope stage and a spectrum was collected. This revealed a strong PL emission peak at 874 nm. A PL lifetime curve was obtained from a cleaved edge of the sample as a test of the TCSPC system. A single exponential fit of the decay curve gave a PL lifetime of 0.5 ns, which matches the findings of Wolford et al. for unpassivated epitaxial GaAs (Wolford et al., 1991).
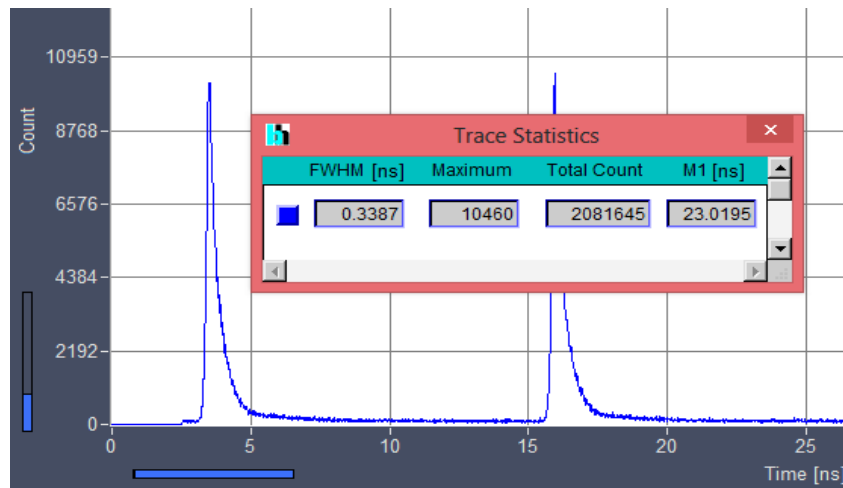
Figure 14: PL decay curve for GaAs test sample using pulsed 445 nm diode laser.

3.1 Location and Description of the Double Defect

After replacing the test sample with sample 1499N, a defect was located by illuminating the sample over a large area with light from an 808 nm diode laser. Using a long pass filter with a cutoff wavelength of 840 nm, defects in the GaAs layer were visible as dark spots on the image from the CCD camera of the microscope. A large doublet defect was located for making PL lifetime measurements (figure 15).

Figure 15: View of a doublet extended defect in GaAs layer of sample as captured by the CCD camera on the LabRam 800 Raman microscope using a long pass filter (cutoff wavelength 840 nm). The sample was illuminated with light from an 808 nm diode laser. The upper defect was used to gather PL lifetime data.
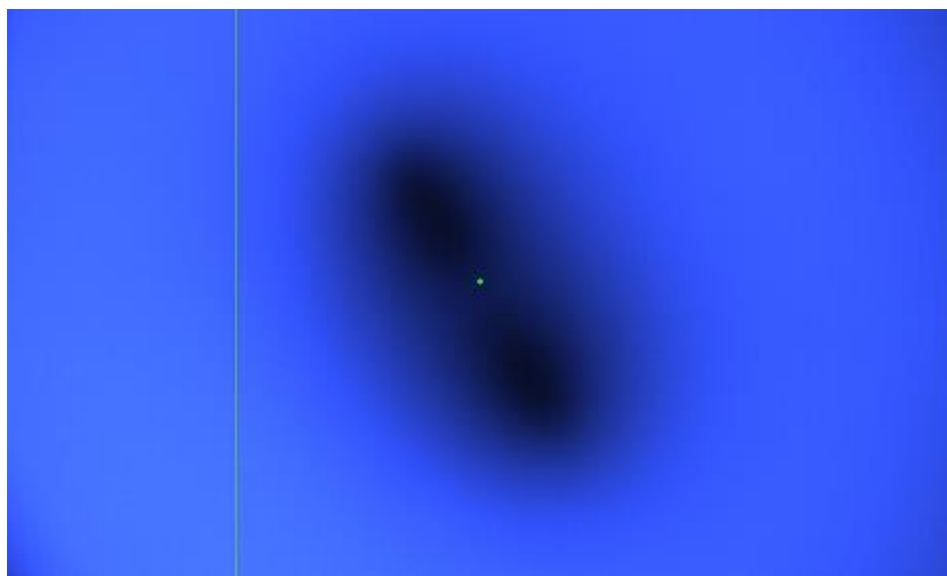
A PL map was made using continuous excitation from a frequency doubled diode pumped Nd:YAG laser ($\lambda = 532$ nm) at 20 mW for the purpose of positioning the upper defect close to the center of the field of view of the microscope (figure 16). The 100x objective (N.A. = 0.9) was used for both the PL mapping and for collection of PL lifetime data.
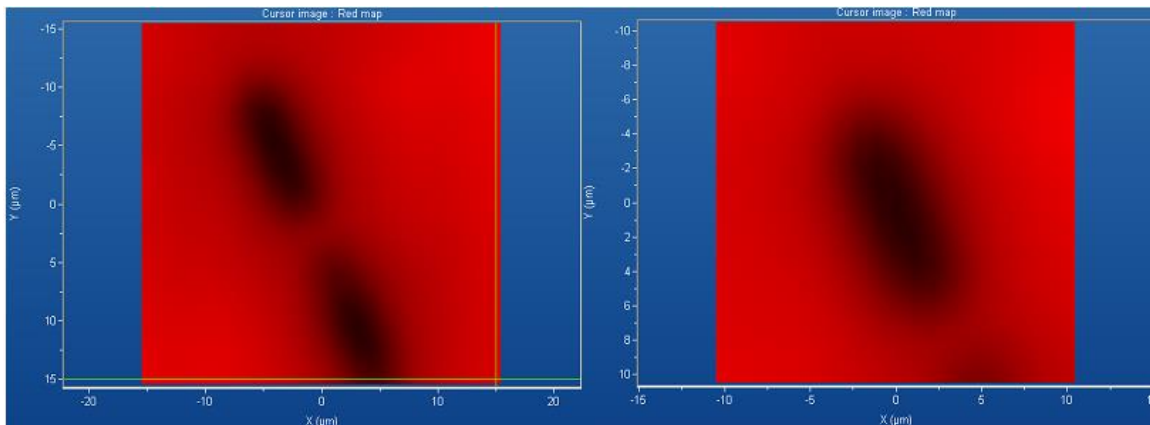
Figure 16: PL map of double defect using 50x objective (left) and PL map of upper defect using 100x objective (right). Approximate defect center on right is at (0,0).

3.3 PL Lifetimes from Two-Point and Line Scan Sampling

Light from the 445 nm pulsed diode laser was then routed through the microscope and onto the sample. The smallest spot size attainable through focusing with the 100x objective was 2.2 μm in diameter as measured on the CCD image. A quick PL spectrum (accumulation time of 3.0 s) was obtained and revealed a broad PL peak with a maximum

at 870 nm (figure 17). The spectrometer remained at this position for the PL lifetime

measurements. All measurements were made at room temperature.
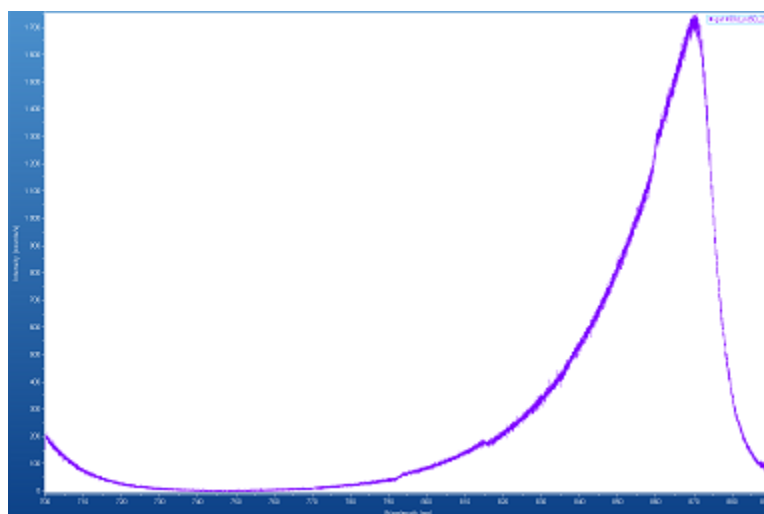
Figure 17: PL spectrum of sample from 700nm to 900 nm. Peak is at 870 nm.

A PL lifetime curve was collected from near the center of the defect using a time

resolution of 12 ps per channel and accumulation time of 100 s. A PL lifetime curve was

then taken at a point approximately 10 µm from the defect center. A comparison of the

two curves is shown in Figure 18. The average background level over the entire

sampling interval is approximately 56 counts. Although this resolution allowed for a

total of 32 curves to be stored in memory, each curve was saved as a separate file to be

processed individually.
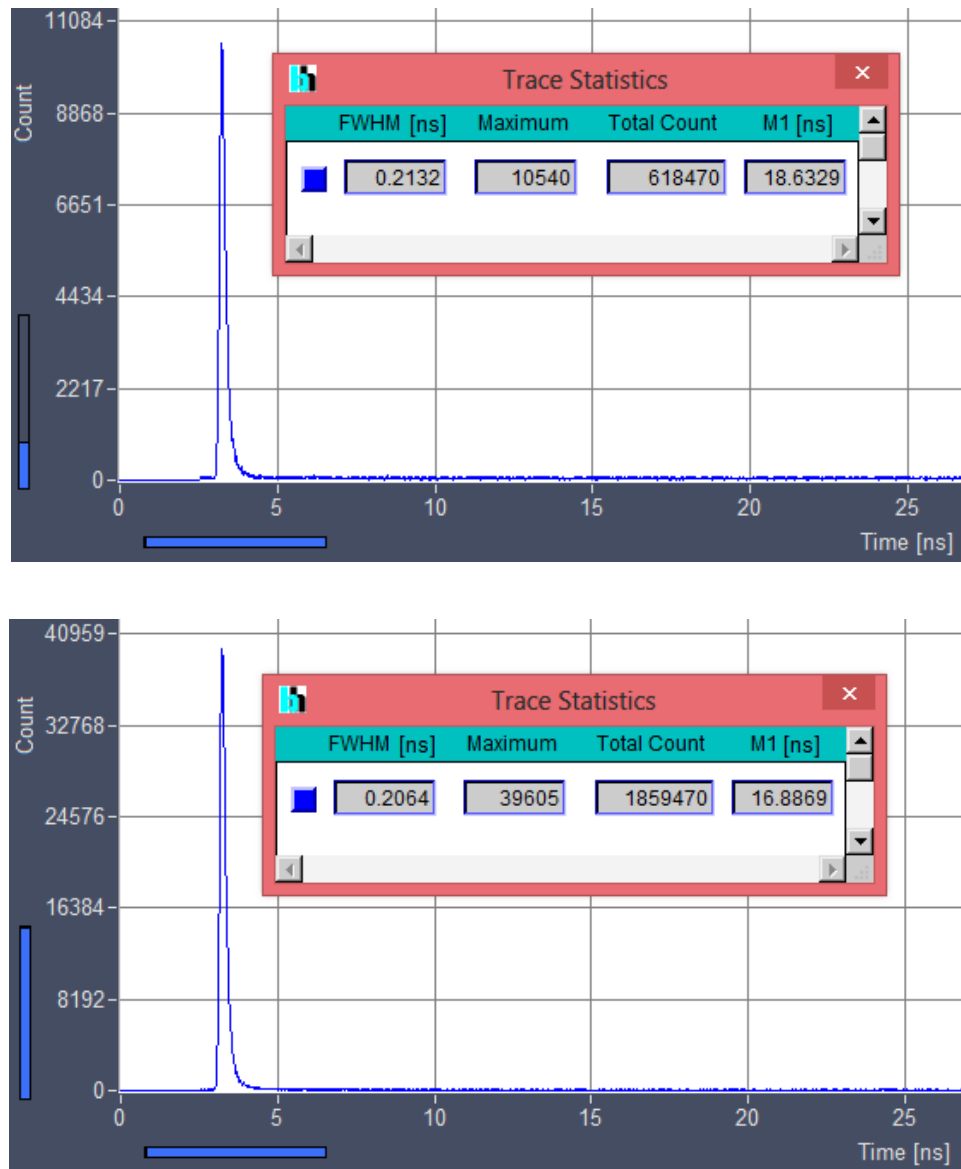
Figure 18: PL decay curves for the double heterostructure GaAs sample with at a point approximately 12 microns from the defect (top) and near the center of the defect (bottom).

The measured PL decay curves are a convolution of the "real" PL dynamics with the instrument response. The full width at half maximum (FWHM) of the measured decay curves is therefore greater than that which would be observed for PL rise and decay alone since the rise time of the laser signal is much shorter than that of the PL

(figure 19). Deconvolution fitting works based on the assumption that the PL lifetime is long compared with the width of the instrument response (Becker and Hickl Handbook,6th Ed.). Lifetimes measured for the defect sample were only 30% longer on average than the instrument response. Values of τ were obtained without deconvolution of the "real" PL decay curves from the measured instrument response function, but rather by using semi logarithmic plots of the raw curves to isolate the exponential tails of each decay which are ideally linear on a semi log scale (figure 20). Non-exponential components made up the first 0.4 ns (400 ps) on average. Single exponential fits of the

form
$$y(t) = ae^{-b(t-t_0)} + y_0 \qquad (7)$$

were performed on the decay curves giving values of $t_0 \sim 25\ ns$ and $y_0 \sim 50.5$ on average. Fits with values of $R^2 \geq 0.994$ or greater were used except at the defect points where the total counts were low and values of $0.991 - 0.993$ represented the best fits in this region. Single exponential fits of the data extracted by this method from both curves are shown in figure 21 and gave values of $\tau = 173$ ps for the distant point and $\tau = 154$ ps for the defect point. Standard error varied with maximum counts and ranged from <1% for distant points and no greater than 5% for the defect centers. Except where noted, all subsequent fits of PL decays are performed in this manner.

GaAs 1499 D1 Decay + IRF

- - - Factory IRF ——— d1 Decay*1.8 ········ Measured IRF
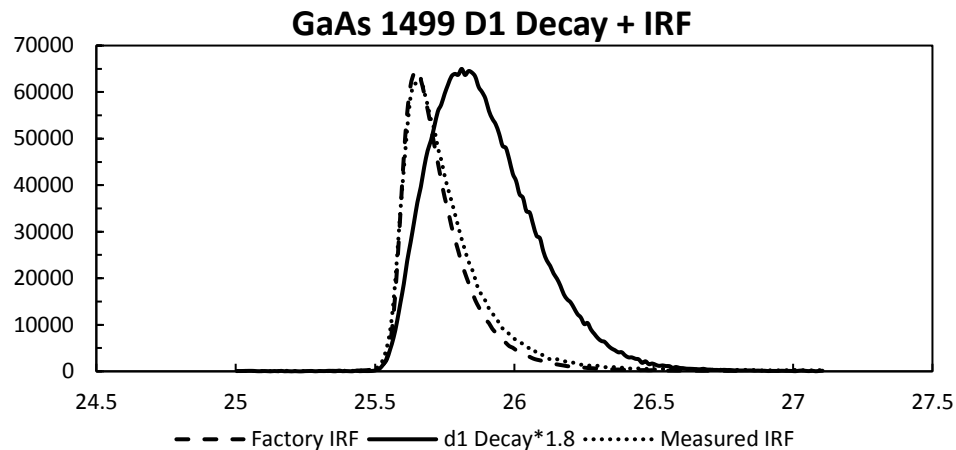
Figure 19: Typical measured PL decay curve with measured instrument response function (IRF). Decay times are less than twice the instrument response time.

GaAs 1499 PL Decay

△ x=0 µm
□ x=-12 µm
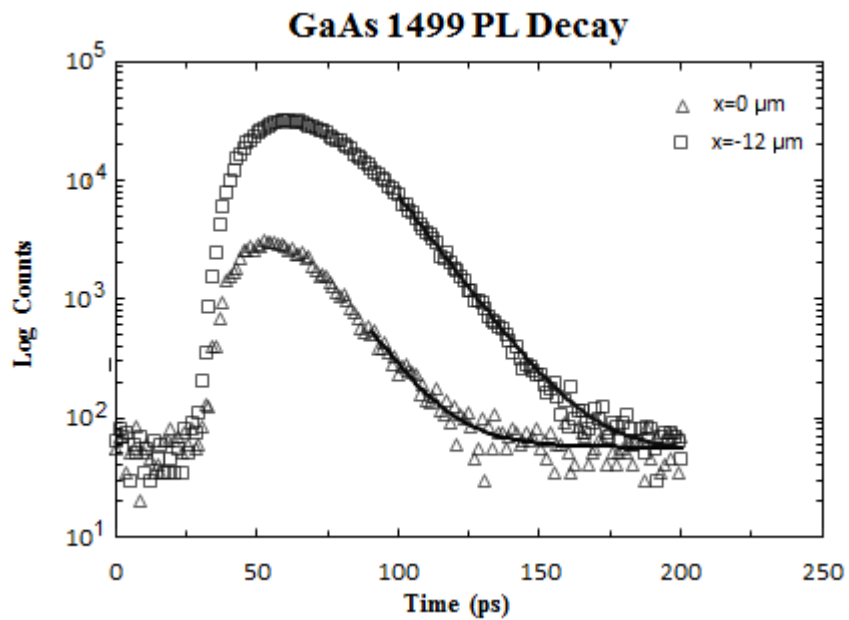
Figure 20: Semi logarithmic plots of PL decay curves from figures 18 and 19 taken in the defect and 12 µm away respectively. All log plots were approximately linear in the region from 90 ps to 170 ps. Solid lines represent mono-exponential fits performed with MATLAB™.
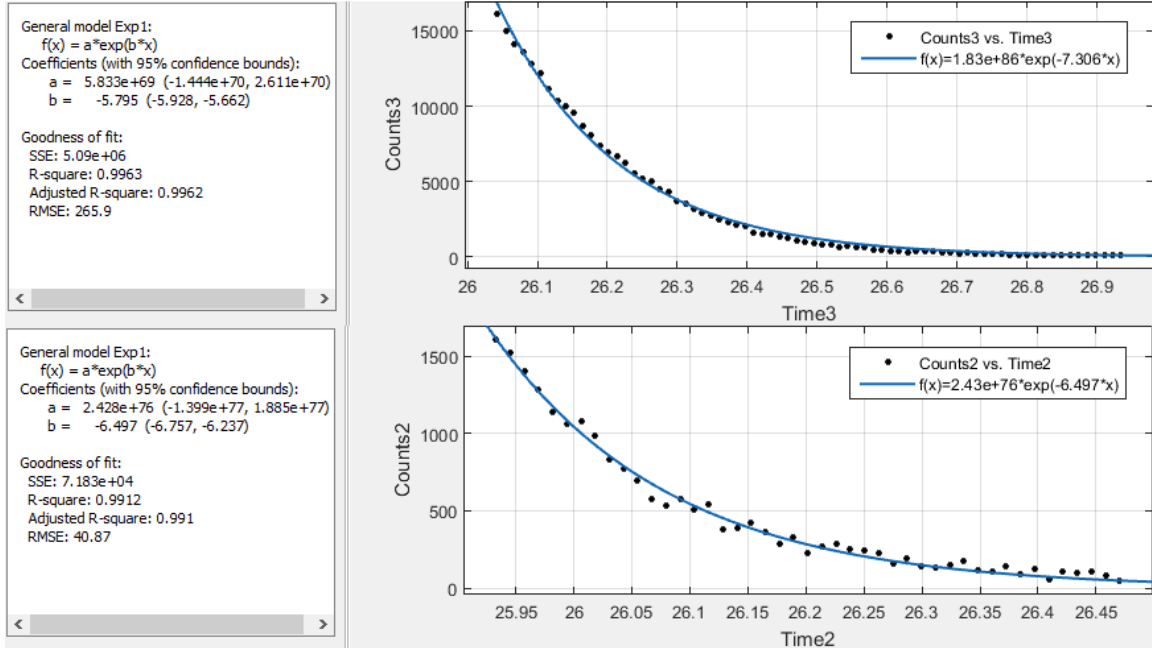
Figure 21: Exponential fits of plots of PL decay curves from figures 18 and 19 performed with MATLAB™ using ns as the default time unit. Starting values were determined from the linear portion of the semi-log plots.

The microscope stage was then positioned so that the laser spot was about 14 microns from the approximate defect center and a PL decay curve was obtained. The stage was then moved in 2 µm increments through software control, with a PL decay curve being collected at each increment over a distance of 20 microns. Time resolution and collection time remained at 12 ps per time channel and 100 s respectively. Eleven curves each were obtained using a 50% neutral density filter, a 25% neutral density filter, and a 10% neutral density filter to attenuate the laser (designated "series g"). This resulted in power densities of 54.0 W/cm², 28.3 W/cm², and 12.1 W/cm² at the sample respectively. These values were determined from the power measured at the objective divided by the spot area ($\pi \times (1.1 \times 10^{-4} \text{ cm})^2$). The energy per pulse was determined from average power by

$$E_p = \frac{Average\ Power}{Repitition\ Rate\ (40MHz)} \tag{8}$$

giving pulse energies from 9.6×10^{-14} J to 2.2×10^{-14} J and peak power densities of 32

KW/cm^2, 16 KW/ cm^2, and 6.5 KW/cm^2. Lifetime data was not collected beyond 6 µm

past the defect center due to time constraints posed by decreasing excitation power to the

sample caused by a slow drift in the laser alignment. The data gathered were sufficient to

construct plots of PL decay full width-half maximum (FWHM), maximum counts, total

counts, and decay time constants vs. position from 14 µm from the defect to just beyond

the defect.

Table 1 shows FWHM, maximum counts, total counts, and computed time

constants for a single line scan across the defect. Because an overflow of the TCSPC

system for maximum counts occurred when using the 50% neutral density filter, these

data were considered unreliable. PL curves collected using the 10 % neutral density filter

provided useful data except for at the defect (x=0) where the signal was too weak. They

are both presented here, however, since the values of FWHM and total counts show a

similar trend to the more reliable values collected using the 25% neutral density filter.

Plots of these values versus position show an unexpected increase in maximum counts,

total counts, and FWHM above background values at locations near the defect, followed

by an expected sharp decrease at the defect center (figure 22). Values of τ were

computed from exponential fits of those decay curves obtained using the 25% neutral

density filter only. These values are also plotted against position in figure 21 and show a

similar increase near the defect.

	Relative Position (µm)	FWHM (ps)	Maximum Counts	Total Counts	Time Constant τ (ps)
ND 10%	-14	381.7	6685	407220	
	-12	351.7	5225	359730	
	-10	393.2	5205	370185	
	-8				
	-6	412	5340	390275	
	-4	387.6	5830	399470	
	-2	366.5	4955	364945	
	0	365	235	5200*	
	2	406.2	5785	403925	
	4	423.6	6225	431165	
	6	394.3	5775	408330	
ND 25%	-14	428.9	49240	2021410	196.7
	-12	417.3	32570	1368310	175.8
	-10	428.6	28760	1270600	175.1
	-8	427.2	29000	1285145	174.2
	-6	448.6	28275	1309400	186.9
	-4	440.5	28200	1299310	187.2
	-2	416.8	24005	1066730	166.9
	0	342.8	3065	297010	160.8
	2	434.3	30760	1378075	180.4
	4	445.9	31265	1446785	196.1
	6	437.9	30300	1369610	183.2
ND 50%	-14	457.4	Overflow	2732460	
	-12	459.8	Overflow	2780950	
	-10	449.4	Overflow	2763340	
	-8	458.9	Overflow	2797640	
	-6	464.6	Overflow	2872695	
	-4	468.3	Overflow	2913810	
	-2	427.9	Overflow	2661040	
	0	344	7565	430975	
	2	463.6	Overflow	2822660	
	4	470.3	Overflow	2905155	
	6	467.2	Overflow	2876460	

* Estimated area under curve

Table 1: FWHM, peak counts, total counts, and decay time constants for a straight line scan across the center of the extended defect. Values of τ are calculated from single

exponential fits of the exponential tails of lifetime curves obtained using the 25% neutral density filter.
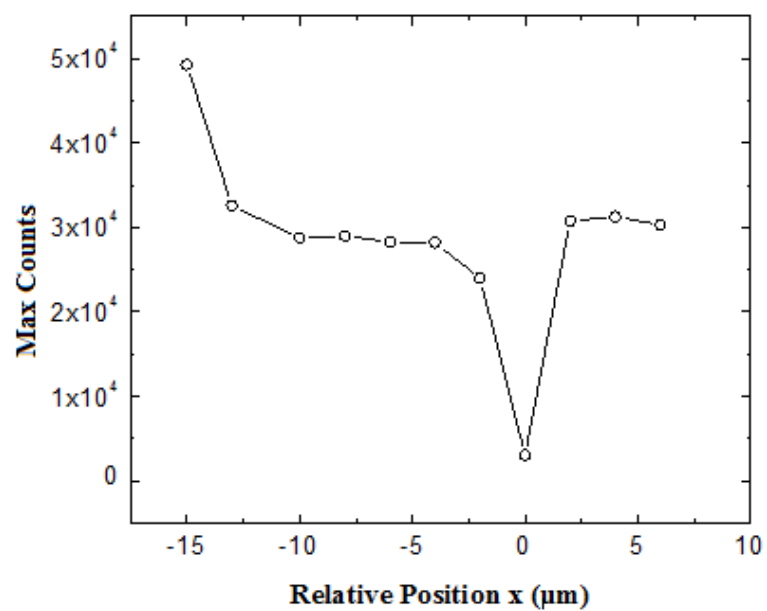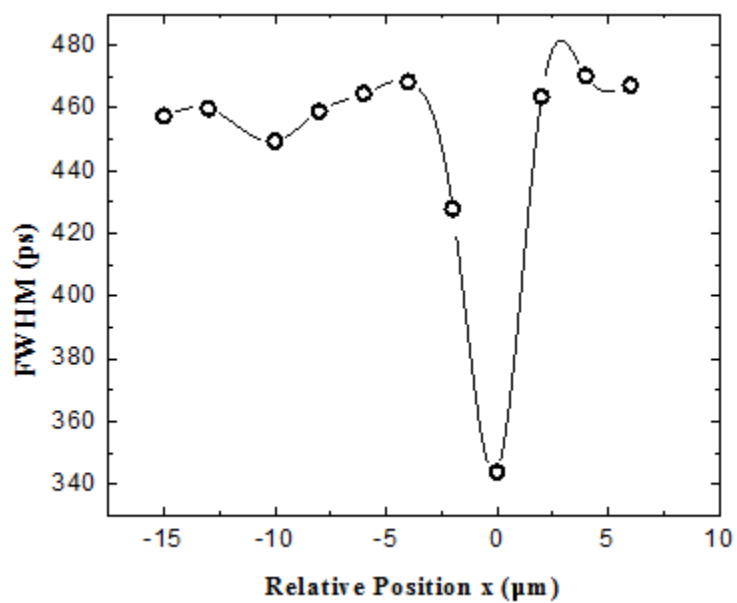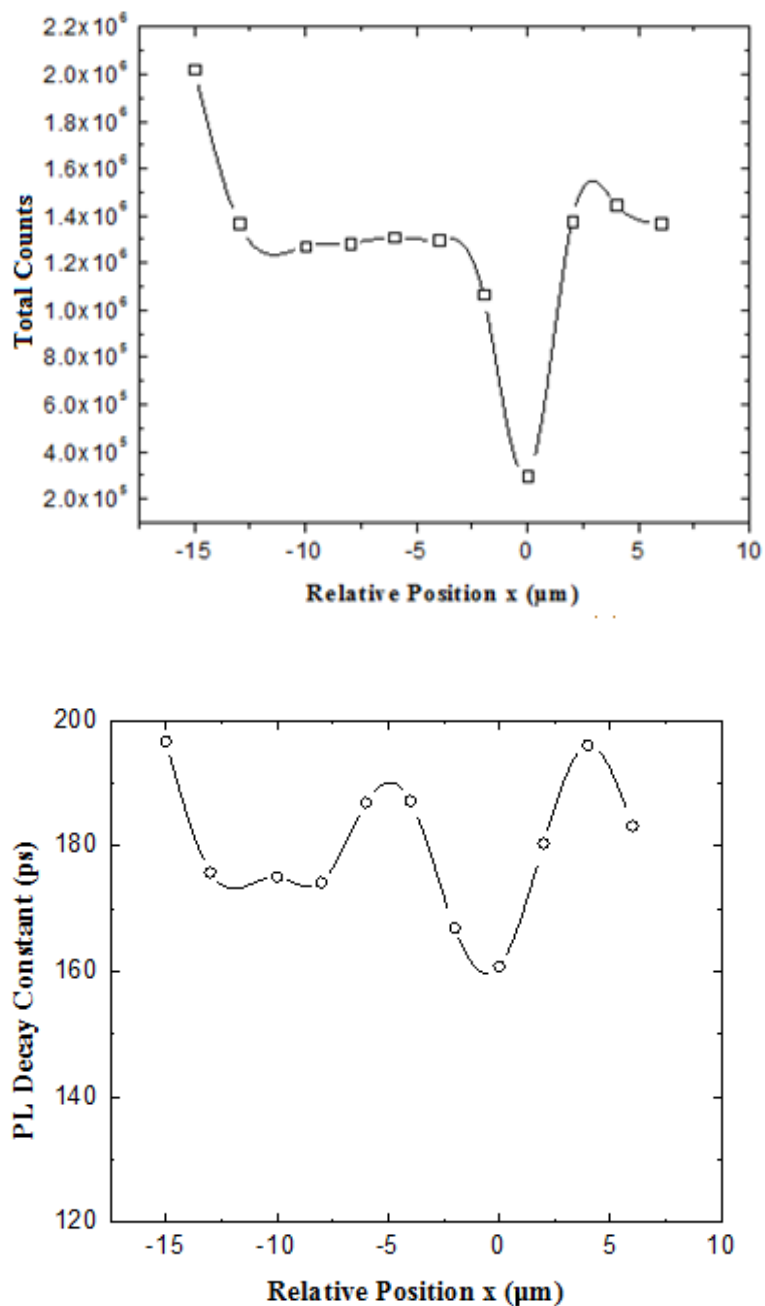
Figure 22: FWHM, maximum counts, total counts, and PL decay time constants from exponential fit of PL decay curves for eleven points along a straight line through the center of the extended defect (center at x=0) at 25% of maximum power. Note higher values of τ on either side of the defect.

Plots of total counts vs. position for all three excitation powers are shown in figure 23 and exhibit a similar pattern of dependence of PL intensity on excitation as seen in the continuous PL maps shown in figure 7. The PL intensity begins to fall off at

slightly greater distance for excitation at 28.3 W/cm^2 than at 54 W/cm^2 but at a lesser

distance for the lowest excitation. This would appear to validate PL intensity

measurements made with the TCSPC system. However, the highest averaged excitation

density used here is 28 times lower than the minimum excitation used in the CW PL

maps of figure 7. This means that the power used here is far below the threshold for

saturating point defects according to the explanation for the sudden decrease in diffusion

length offered by Gfroerer et al. for figure 7d.
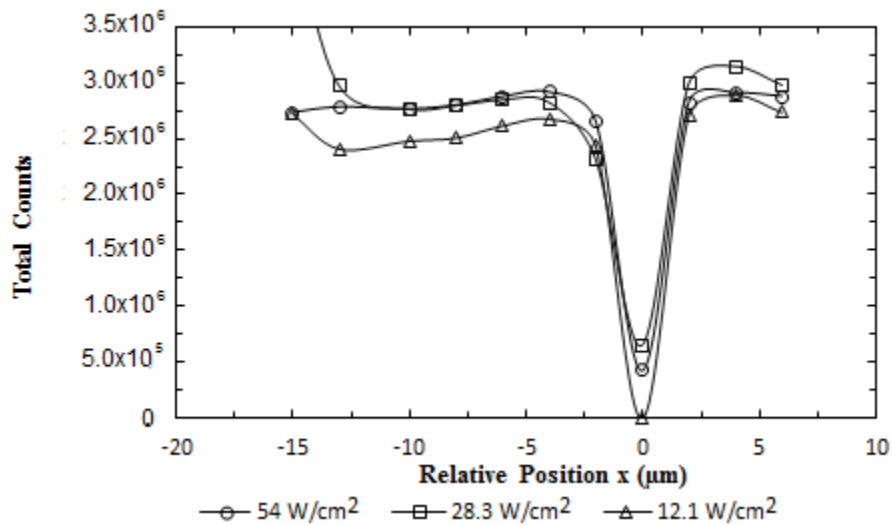
Figure 23: Plot of total counts vs. position for three different excitation power levels.

A second series of PL decay curves (designated as series d) was collected for

comparison of PL lifetimes with those of the first series. To reduce collection time, only

the 25% neutral density filter was used for laser attenuation. This allowed for the

collection of 15 curves in a shorter period of time and thus reduced the impact of

decreasing excitation power on the measurements. Adjustments to laser alignment gave

approximately 37 W/cm^2 at the sample. The time resolution and collection time

remained at 12 ps per channel and 100 s respectively. Table 2 shows FWHM, total

counts, and values of τ from single exponential fits. These values are plotted against relative position in figure 24. The decrease in excitation power (density) was determined to be 41% from photon count rates measured using the LabRam system before and after taking the lifetime measurements. The data are presented here without correction for power loss. Again, an increase in all measured quantities was observed for points near the defect. The increase in total counts in both series implies higher PL intensity which is not seen in previous CW PL maps. The increase in τ near the defect is unexpected since defect related trapping is expected to decrease the free carrier lifetimes. Diffusion of carriers from the excitation volume near the defect is also expected to reduce PL lifetime as well as PL intensity from that region (Gfroerer, Zhang, Wanlass, 2014).

Relative Position (µm)	FWHM (ps)	Maximum Counts	Total Counts	Time Constant τ (ps)
-20	421.8	36140	1526290	184
-18	418.8	36820	1560280	186
-16	415.8	40575	1678435	170
-14	423.5	40145	1692495	167
-12	419.3	43160	1782420	163
-10	424.4	42640	1781075	162
-8	427	42420	1777895	164
-6	427	44080	1862270	179
-4	446.6	46810	2045510	193
-2	460	50935	2243800	201
-1	438.9	49720	2148355	192
0	423.6	46690	1951440	173
1	340.3	6120	393580	152
2	349.1	19055	792605	138
3	412.7	51285	2051355	159

Table 2: FWHM, peak counts, total counts, and decay time constants for a straight-line scan across the center of the extended defect.
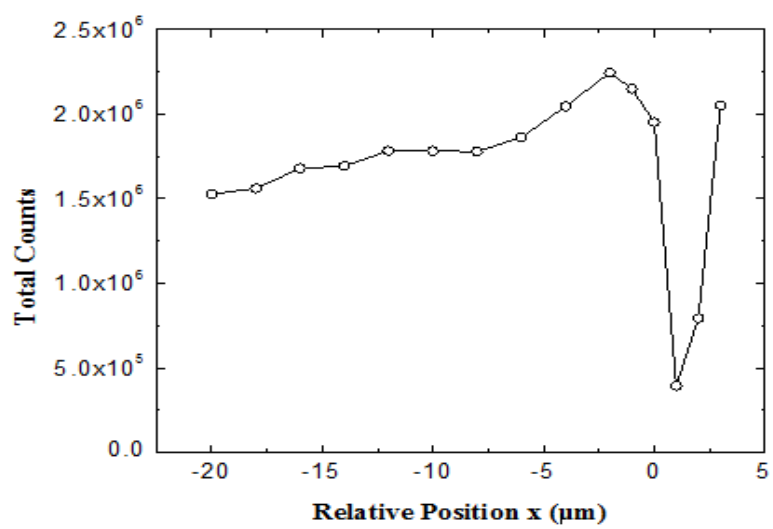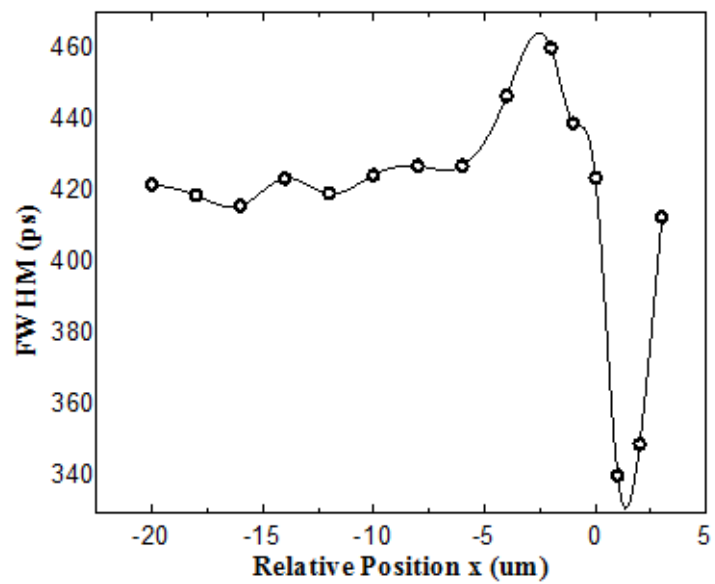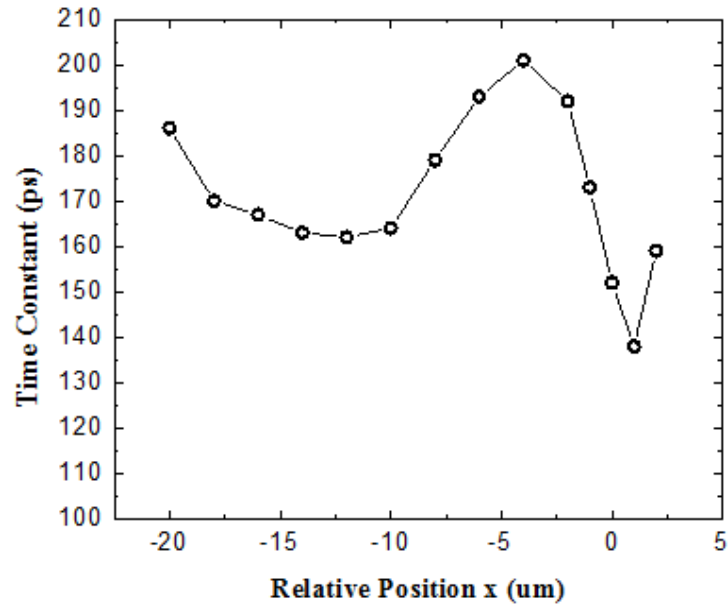
Figure 24: FWHM, total counts, and PL decay time constants vs. position for a linear scan from 20 μm from defect to just beyond defect center (x=2μm).

3.4 Comparison of PL Measurements with Previous Works

Average PL lifetimes taken from the same seven points from each series showed a difference of less than 1.1% between the two series. In both series, values of τ are much shorter than the average minority carrier lifetime of $\sim 10^{-8}$ s in bulk GaAs (Sze, 2009), shorter than the PL lifetime of 2.5 μs for a thick AlGaAs/GaAs/AlGaAs double heterostructure, 2 ns for a bare GaAs surface with an AlGaAs back layer, and even shorter than that of 0.5 ns for an unpassivated GaAs epilayer (Wolford, et al., 1991). They are, however, much longer than those reported for single and two-photon excited fluorescence reported for bulk n-type GaAs doped with silicon (Penzkofer and Bugayev, 1988). According to the findings of Wolford et al., the PL lifetime of this GaAs double heterostructure sample should be on the order of 1 μs, if it were well passivated and had a very low defect density. If the fluorescence lifetime is estimated as

$$\tau_F = \tau_{rad}\eta_{int} \tag{9}$$

where η_{int} is the internal quantum efficiency (Penzkofer and Bugayev, 1988), and the radiative lifetime is assumed to be on the order of 1 μs, then using estimates of radiative efficiency from figure 7d (~0.002 – 0.006, lowest excitation) as a substitute for η_{int} gives a luminescence lifetime range of 2 – 6 ns. However, the current sample, although similar in structure and composition, is not the same as that used by Gfroerer et al. for the PL maps in figure 7 (Gfroerer, 2013). It is the same as that used by Chen et al. for the study of the different excitation geometries mentioned in chapter1 (Chen, 2015) and was known to have a lower PL efficiency than the GaAs/GaInP double heterostructure used in figure 7. This may offer at least a partial explanation for the shorter PL lifetimes observed here in accordance with equation (9). It is also important to note the differences in the manner in which the PL lifetimes were extracted from the PL decay curve in the studies mentioned above. For instance, the "radiative lifetime" reported by Wolford et al was not derived from the early exponential portion of the decay curve but rather from the tail of the decay curve by considering the nonlinear decay dynamics. The rate equation (Eq. 1) can be modified for the case of p-type minorities in an n-type material (Wolford et al., 1991) as

$$\frac{dp}{dt} = -B(np + n_0 p + p_0 n) - \frac{p}{\tau} - \frac{2S}{d}p \tag{10}$$

whose analytic solution yields the time dependent minority carrier density *p(t)* from which the time dependent PL intensity can be derived as

$$I(t) = I_0 \frac{A e^{\frac{-(t-t_0)}{\tau}}}{1 + C\left(1 - e^{\frac{-(t-t_0)}{\tau}}\right)} \tag{11}$$

where C is a measure of the bimolecular component of the decay based on the initial

population of both carrier species (Wolford et al., 1991). This rate equation indicates the

time dependence does not follow the simple exponential decay. Apparently, only after a

considerable delay time when the carrier density becomes small will the simple

exponential decay be restored. However, because the signal has also become very weak

by this time, the initial decay is often used as a measure of PL decay. Although the decay

time extracted may not be the PL decay time strictly speaking, it can still be used for

comparison between a less defective sample (slower decay) and a more defective sample

(faster decay). An attempt to fit the data from figure 20 to Eq. 10 yields lifetimes of

0.163 ps and 0.131 ps at and away from the defect site respectively (figure 25). This is

contrary usual predictions of shorter lifetimes in the defect. Further complication is

added to the data analysis when the PL is measured using point source excitation,

because lateral diffusion, even in the simplest case where C = 0, also affects the PL decay
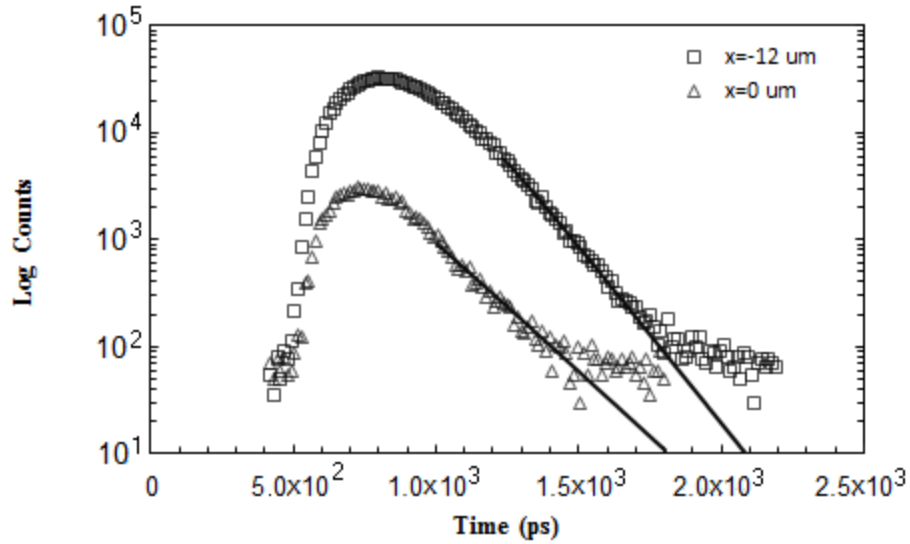
(Wolford, 1993).

Figure 25: Semi-log plots of PL decay curves from figure 20 fit to eq. 10. Solid lines represent best nonlinear least squares fit using MATLAB. Note lifetime in the defect is shown to be longer than at 12 µm distance.

Table 3 shows diffusion lengths calculated from values of τ for series g and d. The diffusivity D is assumed to be spatially uniform in the region and is taken as 200cm^2/s (Sze, 2nd Ed.; Wolford, 1993). This is the value in the bulk and may be quite different near the defect. It has been shown that prolonged exposure to high power excitation changes the physical properties of the defect and suggested that the diffusivity may be changed also (Gfroerer, Zhang, and Wanlass, 2013). Values of the diffusion length calculated using Eq. (5) are about $\frac{1}{8}$ the predicted value using bulk parameters:

$$L_D = \sqrt{\left(2\times10^{10}\,\frac{\mu m^2}{s}\right)\left(1\times10^{-8}\,s\right)} \cong 14\,\mu m \qquad (12)$$

Although diffusion is expected to be reduced by defect related trapping near the dislocation, the values of diffusion length shown here are much lower than expected based on distances of tens of µm observed in the same sample using CW PL mapping.

However, diffusion lengths calculated from contrast profiles of PL maps of the defect site predict diffusion lengths as short as 4 µm for an unmodified defect and 3 µm after the properties of the defect have been altered by long term exposure to high power excitation (figure26). Note that a factor of 2 should be applied to values of "effective diffusion length" in figure 25 given by Gfroerer et al. (Gfroerer, Zhang, and Wanlass, 2013), following the discovery by Chen et al. of a factor of 2 appearing in the contrast function for the 1-D diffusion model in the L/L mode (Chen, 2015). Assuming that the defect under investigation has been altered by repeated exposure to high excitation power, diffusion lengths here are within a factor of 4 of the lowest value for effective diffusion length based on the modified ED in figure 25. This value, which corresponds to an excitation of 1.5 KW/cm^2, represents the decrease in diffusion length at the lowest excitation seen in figure 7 (Gfroerer, Zhang, and Wanlass, 2013). The much lower excitation density provided by the pulsed diode laser used in these experiments may be responsible for the shorter PL decay times by way of lower initial photogenerated carrier densities resulting in even shorter calculated diffusion lengths than those observed in the CW mapping. Further time resolved PL studies at a wider range of excitation powers, including powers up to the those used in previous CW PL mapping, are required to establish a relationship between carrier lifetimes and diffusion lengths near the defect. A series of PL maps taken at decreasing powers will also be required to establish a threshold value at which the increase in PL intensity above background near the dislocation appears. They may also help determine if this observed increase, which appears as a 'halo' around the defect on PL maps, is an actual increase or simply a matter of the background PL decreasing faster with decreasing excitation density than the PL

near the dislocation. Plots of diffusion lengths from table 3 vs. distance from the defect

are shown in figure 27 and show a similar spatial dependence to plots of FWHM and total

counts.

Although the difference in the excitation density may partially explain the

difference in the derived diffusion length, as stated above, the PL lifetimes measured

using the current method (including the effect of lateral diffusion), are not the bulk

lifetime as required by Eq. (5). An explicit modeling of the diffusion-recombination

process in the L/L mode should be carried out for the time dependent PL measurements,

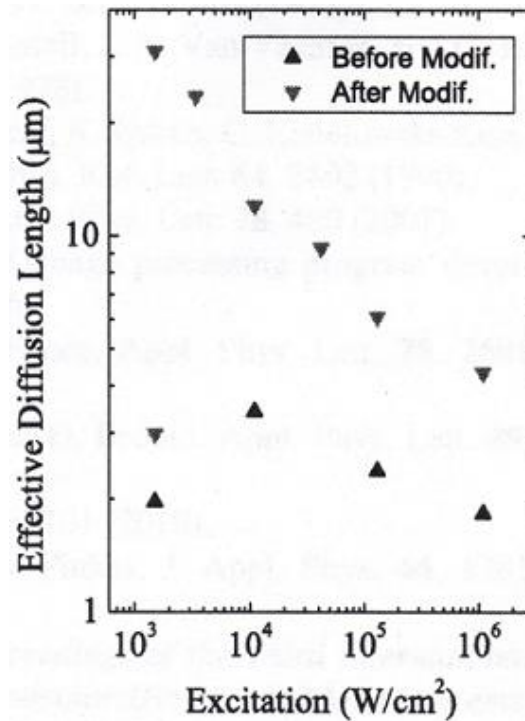in contrast to the CW measurements treated previously (Chen, 2015).

Figure 26:   Effective diffusion length vs. excitation derived from PL map contrast
profiles before and after laser modification (Gfroerer, Zhang, and Wanlass, 2013).

Relative Position x (µm)	Decay Time Constant τ (ps)	Diffusion Length (µm)
-15	196.7	1.98
-13	175.8	1.88
-10	175.1	1.87
-8	174.2	1.87
-6	186.9	1.93
-4	187.2	1.93
-2	166.9	1.83
0	160.8	1.79
2	180.4	1.90
4	196.1	1.98
6	183.2	1.91

g Series

(a)

Relative Position x (µm)	Decay Time Constant τ (ps)	Diffusion Length (µm)
-20	184	1.92
-18	186	1.93
-16	170	1.84
-14	167	1.83
-12	163	1.81
-10	162	1.80
-8	164	1.81
-6	179	1.89
-4	193	1.96
-2	201	2.00
-1	192	1.96
0	173	1.86
1	152	1.74
2	138	1.66
3	159	1.78

d Series

(b)

Table 3: Diffusion lengths calculated from values of τ obtained from single exponential fits of the tails of decay curves from g and d series measurements.
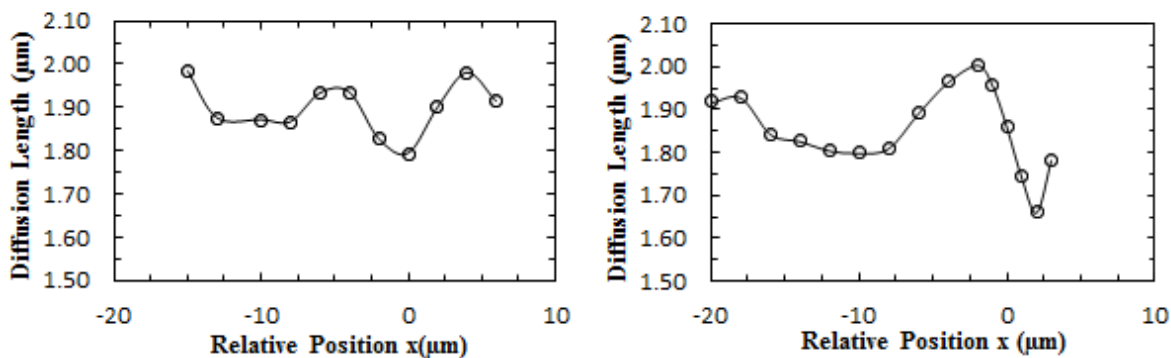
Figure 27: Plots of calculated diffusion lengths vs. distance from the defect center (x = 0 µm on left, x = 2µm on right). The offset of the defect center on the right is a result of difficulty in positioning the sample with no visual reference for the defect.

The low excitation used for collecting the PL data presented here is believed to be at least partially responsible for the difference between PL lifetimes and diffusion lengths

from table 3 and diffusion lengths from previous CW PL maps (as in figure 7).

Excitation power used for series d above is lower than the minimum excitation from

figure 7 by a factor of 53. A more extensive series of PL lifetime measurements as well

as PL maps, both taken over a larger array of excitation densities, will be required for

more comprehensive modeling of the charge carrier behavior in the region of the

dislocation.

3.5 Line Scan with PL Mapping; Appearance of the 'Halo' Effect

A third series of PL decay curves was obtained on a separate occasion with better

laser alignment and more power at the sample (series k). The increase in power made it

possible to obtain PL maps with the pulsed 445 nm diode laser using a 50% neutral

density filter giving an average power of 3.85 µW or approximately 100 W/cm^2 at the

objective with a spot radius if 1.1 µm. PL maps were initially made with a CW diode

pumped Nd:YAG laser (λ=532 nm) at low power for comparison . Power was

approximately 3.3µW or 160 W/ cm^2 at the objective with a 0.4 µm spot radius. Figure

28 shows PL maps made with both lasers. Note the bright areas around the defect which

were not seen previously at higher excitation power (Chen, 2015). This is in agreement

with the plots of counts vs. position from the two previous line-scan series of PL lifetime

curves in which the photon counts increase near the defect. The slightly lower spatial

resolution of the map made with the pulsed diode laser is due to its larger spot size.
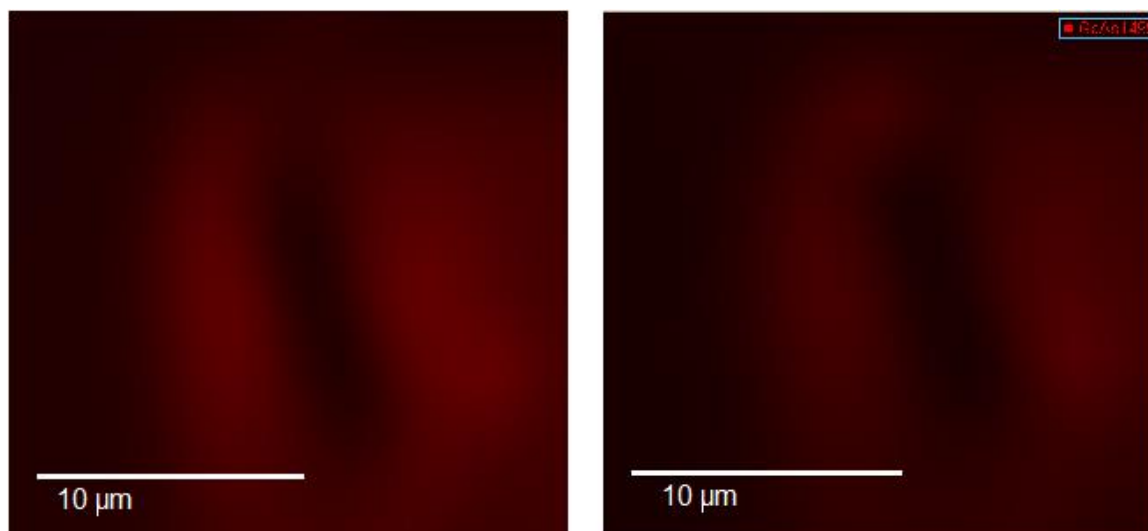
Figure 28: PL Map of defect with CW excitation from diode pumped Nd:YAG laser at 532 nm (left) and with pulsed excitation from 445 nm diode laser (right). The decrease in spatial resolution on the right is attributed to the larger spot size of the pulsed blue diode laser.

PL lifetime curves were then obtained using the 10% neutral density filter in the laser path to avoid overflow of the SPC system which occurred with the 25% and 50% filters at the higher laser power. Time resolution and collection time were 12 ps per channel and 100 seconds respectively. Table 3 shows FWHM, maximum counts, total counts, and PL decay time constants for 19 points from a linear scan across the defect. The stage was moved in increments of 2 µm for each point with the exception of those points from x= -4 µm to x=4 µm, for which the step size was 1 µm. This was done in an attempt to capture more detail near the defect. The range was chosen based on previous scans and the size of the bright areas in the PL maps.

Relative Position (μm)	FWHM (ps)	Maximum Counts	Total Counts	Time Constant τ (ps)
-16	403	14280	668905	146.1
-14	379.4	10155	526860	146.7
-12	381.8	8270	464830	142.0
-10	375.7	9465	493925	153.2
-8	408.5	10945	569760	142.2
-6	433.7	11785	633285	179.0
-4	408.5	10840	574320	159.1
-3	394.7	9015	496765	156.6
-2	369.3	7065	411640	142.0
-1	332.4	2245	255860	152.1
0	336.4	540	202125	220.8
1	366	4930	342290	159.4
2	409.4	7190	437775	175.7
3	406.7	7390	455045	165.5
4	407.3	6585	423010	165.6
6	388.8	5605	372355	178.5
8	387.5	4870	351395	156.7
10	368.3	3820	310525	145.7
12	361.1	3020	281100	158.2

Table 3: FWHM, counts, and PL decay time constants for decay curves taken from a linear scan across the defect. The defect center is at x=0.

Again, a decrease in excitation power was observed over the course of the scan. Figure 29 shows plots of FWHM, counts, and decay constants versus relative position with the defect center near zero. Given the shape of the plots of counts versus position in previous scans, the power loss is assumed to be linear. Figure 30 shows a plot of the corrected total counts based on a 43% power reduction at the sample during the scan.
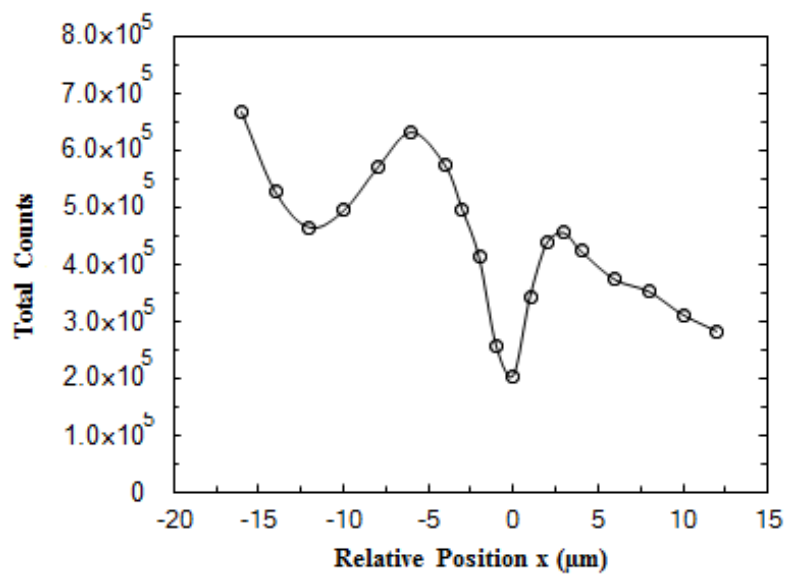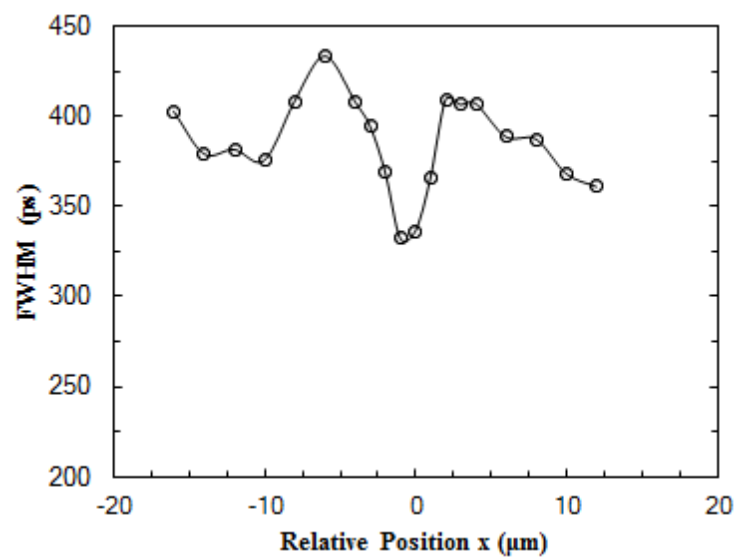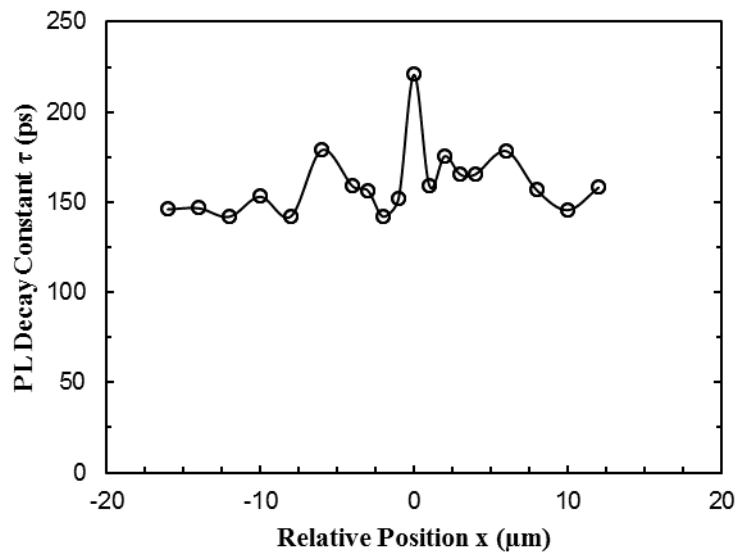
Figure 29: FWHM, maximum counts, total counts, and PL decay time constants across the defect with defect center at x=0.
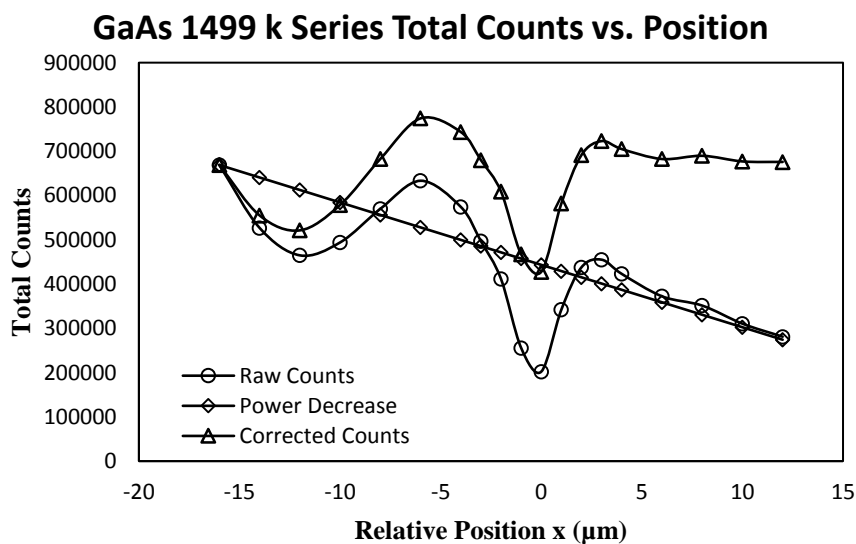

Figure 30: Total counts vs. position with correction for 43% power loss at the sample.

Although the available laser power was higher for this series, the use of the 10% neutral

density filter in the laser path resulted in lower counts for points within the defect

accompanied by a lower signal to noise ratio. This produced poor fitting results for the

decay curve in the defect, giving values of τ that were inconsistent with the trend

observed in the first two series. Figure 31 shows semi-log plots of PL decay for 4 points

near the defect including the defect center. Using the same nonlinear least squares

method used for the plots in figure 22 was less successful as is evident from the abrupt

departure from the true exponential at larger values of t. However, since this pattern is

consistent among several decays, it could be evidence of a more complex PL decay for

very low carrier concentration. The unexpected increase in lifetime in the defect could

also be a real consequence of the low excitation density since there is no lateral diffusion
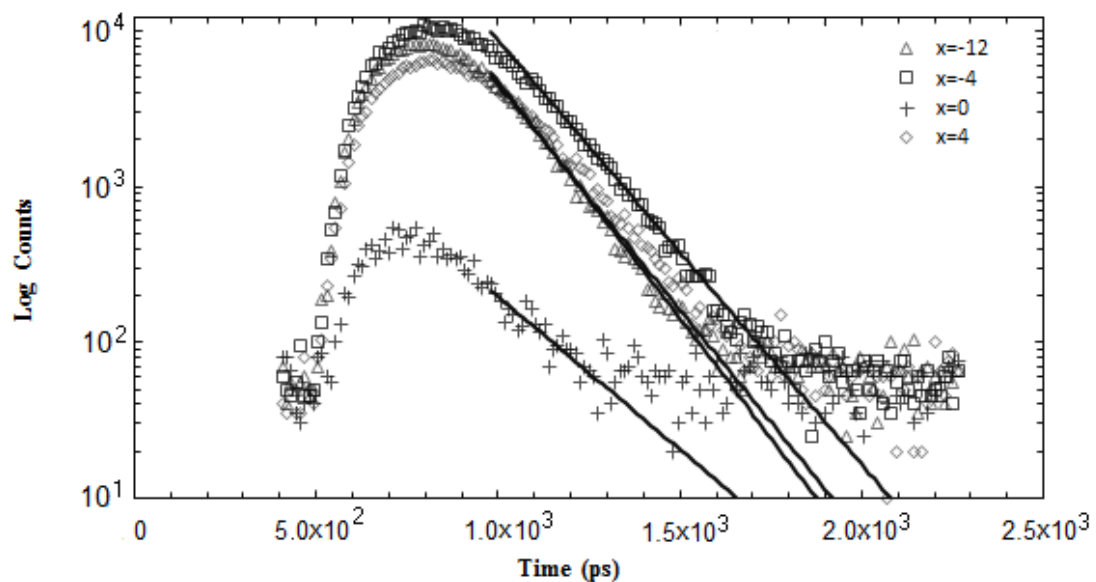
there.

Figure 31: Semi-log plots of counts vs. time for four points near and in the defect. Solid
lines represent attempts at nonlinear least squares fitting using MATLAB^{TM}.

Because of the difficulties in fitting the decays from this series, calculations and maps

with τ use those values obtained with the first and second series. Because of the ability to

record PL maps with the k series, these data are used for comparison of the spatial

dependence of intensity with that of the previous series.

Using the corrected values of total counts, a 1-D map of PL intensity was

constructed for comparison with PL maps obtained using the LabRam 800 Raman

microscope. Although much lower in resolution (19 pixels vs. 314 pixels), the linear map

shows a visual trend that is similar to the 2-D PL map when superimposed over the

approximate region in which the linear scan was made (figure 32).

Figure 32: 1-D PL intensity map made with TCSPC system superimposed on 2-D PL
map made using LabRam 800 Raman microscope.

The very low power used here may also be responsible for (at least the appearance

of) the higher PL intensities measured near the defect. At extremely low carrier densities,

the competition between point defects and the extended defect seems to shift to favor

radiative recombination just outside the dislocation. Modification of the extended defect

by exposure to high power excitation is known to increase the diffusion length by as

much as 3 times that of an unmodified defect (Gfroerer, Zhang, and Wanlass, 2013). Localized heating in the extended defect from high power excitation may also be responsible for eradicating some non-impurity point defects (such as grain boundaries) through annealing and thus improving the crystal quality near the dislocation and increasing the likelihood of radiative recombination in that region. However, while this may account for the increase in PL intensity near the defect, it should also result in greater diffusion lengths due to fewer point defects to obstruct diffusion.

The 1-D PL intensity map demonstrates the ability of the TCSPC system to reliably reproduce the type of measurements made with the LabRam 800 system. Improving image resolution is a simple matter of sampling a larger number of closely spaced points per scan, while spatial resolution will be improved with reduction of the excitation spot size. Two-dimensional mapping is also within the capabilities of the system. Temporal resolution and greater sensitivity give the TCSPC system its greatest advantage over the Raman system's CCD array detectors and recording method.

A low-resolution PL lifetime map was constructed using values of τ from the first two series (figure 33). While very little variation is visible in most of the lifetime map, it does show that the PL lifetimes exhibit a similar pattern of spatial dependence as the lifetime and FWHM values (figure 33), as is evident form the darker regions at the far left and in the defect.

g Series FWHM

g Series τ

-14 -12 -10 -8 -6 -4 -2 0 2 4 6

Relative Position x (um)

200 ps

190 ps

180 ps

170 ps

d Series FWHM

d Series τ

-20 -18 -16 -14 -12 -10 -8 -6 -4 -2 -1 0 1 2 3

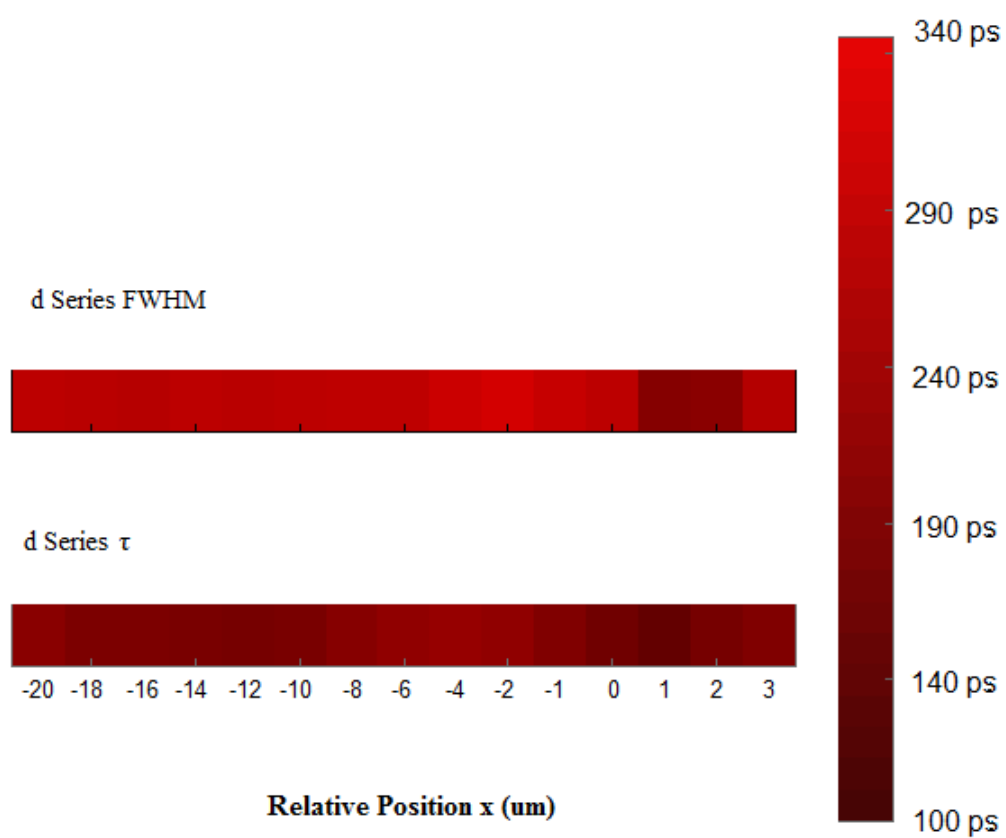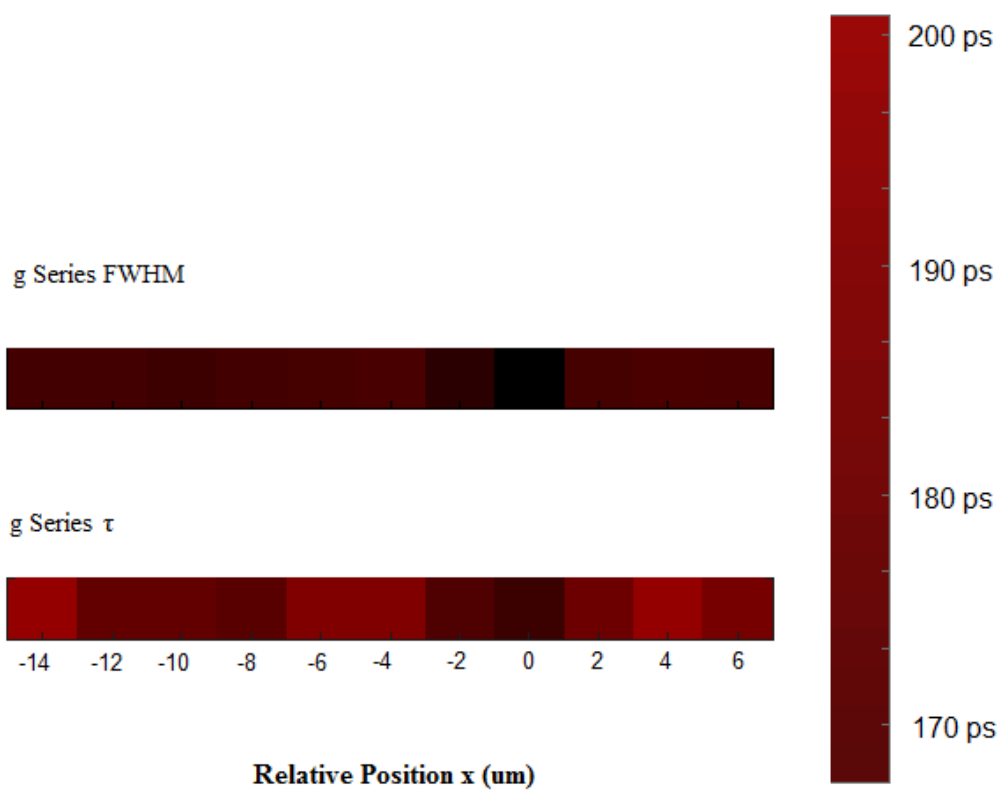**Relative Position x (um)**

340 ps

290 ps

240 ps

190 ps

140 ps

100 ps

Figure 33: 1-D PL lifetime maps from series g and d compared with maps of values of decay FWHM. Defect center is at x=0 µm for series g and x≅1 µm for series d.

Figure 33 illustrates the feasibility of using this system for time and spatially resolved PL mapping/imaging. The goal of acquiring images of spatial resolution comparable to that of PL maps obtained with the LabRam 800 Raman microscope is hindered only by the laser spot size, while acquiring images of comparable field size is limited by the time required to operate the system manually and the accumulation time required given the low excitation power. The time required to collect PL curves for 19 points using 100 second accumulation time was approximately 50 minutes. The time required to obtain a 1-D map of the same resolution as the 2-D PL map (314 pixels) was computed to be about 14 hours whereas acquiring a 314 ×314 pixel 2-D lifetime image would require more than 4000 hours. While this is hardly practical, automation of the system, the use of a pulsed laser with more available power, and a more sensitive detector (which could allow for shorter integration time) could make time efficient 2-D PL lifetime imaging possible with the present TCSPC system and confocal microscope. A wider range of excitation power is needed for both further investigation of the low carrier density phenomena and PL lifetime studies at excitation densities approaching those of previous CW PL mappings. However, care must be taken to avoid modification of the defect and alteration of the carrier dynamics which accompany prolonged exposure to high excitation density. The availability of a more sensitive detector with lower dark counts is the most desirable way to improve overall efficiency of the system. Spatial resolution will be improved by the addition of the single mode fiber system for laser coupling to

improve the excitation beam quality. Temperature dependent PL lifetime studies will allow for a more detailed examination of charge carrier dynamics and recombination kinetics in the vicinity of the extended defects and will become available with the addition of the proposed cryostat and temperature controlled stage.

CHAPTER 4: CONCLUSION

4.1   Summary of System Tests and Experimental Results

The effectiveness of a system with low initial cost for obtaining time and spatially

resolved PL data has been demonstrated. The ability to construct PL lifetime as well as

PL intensity maps from the data gathered with this system has also been demonstrated.

Although the spatial resolution is currently not as high as that of previous work by this

group in CW PL mapping, the resolution is sufficient to locate the defect and discern

patterns of PL intensity which are compatible with those seen in previous CW PL maps.

Although PL lifetimes were much shorter than expected, the data and the images thus

obtained clearly show a significant difference in PL lifetime in the defect which is

sufficient to determine the position of the defect center. While simple single exponential

fits reveal a decrease in PL lifetimes in the defect, fits based on a more complex model

that involves recombination and bimolecular rate terms show longer lifetimes in the

defect. It is obvious that even a more sophisticated mono-exponential function with both

intensity and temporal offsets is insufficient to describe the carrier behavior both in the

presence of defects and under low injection conditions. While the fitting function based

on the more comprehensive rate equation yields better fits, the results are contrary to the

more common observations of relative carrier recombination times in the dislocation.

The results here demand a closer examination of possible processes that occur in the ED

and to what extent the lack of lateral diffusion in the model plays a role in the change in

PL lifetime there.

The system described here has the capabilities to conduct such a detailed

examination. With the ability to obtain Raman and PL spectra, as well as time and

spatially resolved PL mapping, this system has the ability to study the carrier phenomena in greater detail than any single method alone. Superior to contact methods (especially in the low injection regime), the near IR to UV and wide power capabilities of this system leave little to desire for optical measurements. The addition of sample temperature control will be of great benefit, and may allow determination of the energy position of trap states in the band gap of this and similar semiconductor materials. This, in turn, could make possible the detailed mapping of states within an extended defect like the one in the present sample.

Operation of the two systems independently, while slow, does not appear to diminish the reliability of the data acquired. Temporal resolution of the TCSPC system was sufficient to differentiate between PL from points outside the defect and in the defect. Difficulty in achieving a smaller laser spot size was the main impediment to achieving a spatial resolution comparable to that of the previous CW PL maps (of less than 1 um). Proof of concept is clearly demonstrated, however, and ongoing efforts will be made to improve the spatial resolution of the system with the addition of a single mode fiber coupling system for the existing laser. Addition of a wider variety of lasers with different wavelengths, pulse durations, polarized output, higher average power, and TEM_{00} output will greatly expand the capabilities of the system and would likely yield results comparable to TRPL imaging systems of much greater cost.

4.2   Other Applications

TPRL has become a popular tool for the study of charge carrier behavior in a wide range of materials. Spatially mapped TPRL eliminates some of the ambiguities of spatially resolved or time resolved PL when used separately. With additional automation and an increase in spatial resolution, this system will be a valuable tool for the study of charge carrier dynamics in a host of materials, including various nanostructures, quantum wells, quantum wires, and quantum dots as well as bulk and structured semiconductors.

4.3   Future Work

The continuation of this project will be of great importance to this group for further material properties research. The system used here is very versatile given its piecemeal nature. However, resources exist to combine the individual components into an integrated system. The ambitious experimenter could make use of the pinout diagrams, address information, and control signal information provided by Becker and Hickl (Becker and Hickl TCSPC Handbook, 6th ed.) to construct a user interface and software. Although lowest in cost, this would be more difficult and time consuming. Dynamic Link Libraries are available from Becker and Hickl, as well as software drivers for the development of user specific software using LabView™. The addition of the Becker and Hickl stepper motor controller for the microscope stage would allow the user to conduct all operations from a single computer console. Processing of data can also be integrated into such a system using built-in processing features of LabView™ or linking in modules written in other programing languages such as C and C^{++}.

The proposed addition of a cryostat and temperature controlled sample stage will allow investigation of the temperature dependence of the multitude of processes that influence charge carrier generation and recombination in semiconducting materials, and

their respective lifetimes, as well as transport characteristics. PL data on a larger variety

of samples with different but well known doping compositions, doping levels, defect

densities, and structural parameters will be needed to address the complex dynamics of

charge carriers in materials such as those in 'real world' devices. The extended defect,

although normally an undesirable flaw, can serve as a built-in tool for the study of carrier

behavior once its properties and influence are better understood. Just as much has been

learned about the atom from spectroscopy and much has been learned about chemical

kinetics from luminescence lifetimes, PL studies of semiconductors should provide a

rigid foundation upon which to build a better understanding of their complex nature.

REFERNCES

Becker, W., "The bh TCSPC Handbook", 6th ed. Becher and Hickl GmbH, December
        2014

Chen, Fengxiang, Zhang, Yong, Gfroerer, T.H., Finger, A.N., and Wanlass, M.W. 2015.
        "Spatial Resolution Versus Acquisition Efficiency in Mapping an Inhomogeneous
        System with Species Diffusion." Scientific Reports, 5:10542, DOI:
        10.1038/srep10542

Fluegel, B., Alberi, K., DiNezza, M.J., Liu, S., Zhang, Y.-H., and Mascarenhas, A., 2014.
        "Carrier Decay and Diffusion Dynamics in Single-Crystalline CdTe as Seen via
        Microphotoluminescence." Physical Review Applied **2,** 034010 (2014) DOI:
        10.1103/

Fox, Mark, "Optical Properties of Solids", Second ed. Oxford University Press, 2010,
        2012, 2013, ISBN 978-0-19-957337-0

Gfroerer, T.H. Zhang, Yong Wanlass, MW. 2013. "An Extended Defect As A Sensor For
        Free Carrier Diffusion in a Semiconductor." Appl. Phys. Lett. **102**, 012114
        (2013); doi: 10. 1063/1.4775369

Gubanov, Alexander, Polojarvi, Ville, Aho, Arto, Tukiainen, Antti, Tkachenko, Nikolai,
        and Guina, Mircea. 2014. "Dynamics of time-resolved photoluminescence in
        GaInNAs and GaNAsSb solar cells." Nanoscale Research Letters 2014 **9**:80;
        doi:10.1186/1556-276X-9-80.

Metzger, W.K., Ahrenkiel, R.K., Dippo, P., Geisz, J., Wanlass, M.W.,and Kurtz, S. 2004.
        "Time- Resolved Photoluminescence and Photovoltaics". 2004 Conference Paper,
        NREL/CP-520-37028 January 2005 Presented at the 2004 DOE Solar Energy
        Technologies Program Review Meeting, Oct 25-28, 2004, Denver, Colorado

Penkofer, A., and Bugayev, A., 1988. "Two Pohoton absorption and Emission Dynamics
        of Bulk GaAs." Optical and Quantum Electronics 1989 **21** 283-306

Saleh, B.E.A., and Teich, M.C., "Fundamentals of Photonics", Second ed. Copyright
        2007 by John Wiley and Sons, Hoboken, NJ, ISBN 978-0-471-35832-9

 PhysRevApplied.2.034010

Sze, S. M., *Physics of Semiconductor Devices,* John Wiley and Sons, N.Y., 1981

Wolford, D.J., Gilliland, G.D., Kuech, T.F., Smith, L.M., Martinsen, J., Bradely, J.A.,
        and Tsang, T.F., Venkatasubramanian, R., Ghandi, S.K., and Hjalmarson, H.P.
        1991. "Intrinsic Recombination and Interface Characterization in 'Surface Free'

GaAs Structures." J. Vac. Sci. Technol. Jul/Aug 1991 **B** 9 (4)